Adsorption of Xyloglucan onto Cellulose and Cellulase onto Self-assembled Monolayers

Chen Qian

Thesis submitted to the faculty of the
Virginia Polytechnic Institute and State University
in partial fulfillment of the requirements for the degree of

Master of Science
in
Chemistry

Maren Roman, Chair
Alan R. Esker, Co-Chair
Hervé Marand

April 19, 2012
Blacksburg, VA

Keywords: cellulose thin films, xyloglucan, cellulase, self-assembled monolayers, adsorption

Adsorption Studies of Xyloglucan onto Cellulose and Cellulase onto Self-assembled Monolayers

Chen Qian

ABSTRACT

Adsorption of xyloglucan (XG) onto thin desulfated nanocrystalline cellulose (DNC) films was studied by surface plasmon resonance spectroscopy (SPR), quartz crystal microbalance with dissipation monitoring (QCM-D), and atomic force microscopy (AFM) measurements. These studies were compared to adsorption studies of XG onto thin sulfated nanocrystalline cellulose (SNC) films and regenerated cellulose (RC) films performed by others. Collectively, these studies show the accessible surface area is the key factor for the differences in surface concentrations observed for XG adsorbed onto the three cellulose surfaces. XG penetrated into the porous nanocrystalline cellulose films. In contrast, XG was confined to the surfaces of the smooth, non-porous RC films. Surprisingly surface charge and cellulose morphology played a limited role on XG adsorption.

The effect of the non-ionic surfactant Tween 80 on the adsorption of cellulase onto alkane thiol self-assembled monolayers (SAMs) on gold was also studied. Methyl (-CH_3), hydroxyl (-OH) and carboxyl (-COOH) terminated SAMs were prepared. Adsorption of cellulase onto untreated and Tween 80-treated SAMs were monitored by SPR, QCM-D and AFM. The results indicated cellulase adsorption onto SAM-CH_3 and SAM-COOH were driven by strong hydrophobic and electrostatic interactions, however, hydrogen bonding between cellulase and SAM-OH was weak. Tween 80 effectively hindered the adsorption of cellulase onto hydrophobic SAM-CH_3 substrates. In contrast, it had almost no effect on the adsorption of cellulase onto SAM-OH and SAM-COOH substrates because of its reversible adsorption on these substrates.

ACKNOWLEDGMENTS

First of all, I owe my deepest gratitude to my advisors, Prof. Maren Roman and Prof. Alan R Esker. It is an honor for me to work in Prof. Roman's and Prof. Esker's groups and this thesis would not have been possible without their support and guidance during my research. I greatly appreciate the tremendous time and effort they invested for improving my research skills and motivating me to understand my subjects in a much deeper level. Beyond supervising me on my laboratory research, Dr. Roman and Dr. Esker also kindly and patiently improved my language and communication skills, which is critical for international students. I am also very grateful to my committe member: Prof. Hervé Marand, for helping me building a solid fundation in polymer physics. Prof. Marand is always open for discussions even though he is quite busy and has limited free time. Additionally, I appreciate the useful suggestions and comments provided by Prof. Kevin J. Edgar during my seminar.

I would like to thank Yafen Zhang in Prof. John R. Morris' group for her suggestions in preparing self-assembled monolayers.

I would like to thank my many colleagues, Dr. Feng Jiang, Dr. Hezhong Wang, Dr. Fernando Navarro, Shuping Dong, Xinyi Tan, Jung Ki Hong, and Kyunghee Kim in Dr. Roman's lab, Dr. Zelin Liu, Dr. Joshua Kittle, Dr. Xiaosong Du, Dr. Yang Liu, Xiao Zhang, Chao Wang, Ying Ni, and Sumin Shen in Prof. Esker’s lab, for their training in using the instruments and various discussions. I want to thank Dr. Bin Li, Dr. Carter Fox, Daiqiang Xu, Siddhesh Pawar, Haoyu Liu, Xueyan Zheng, Ruoran Zhang, and Junia Pereira in Prof. Edgar’s lab for their help in my projects.

Last but not least, I would like to thank my parents, Junhua Qian and Jianhua Wang, for their unconditional love and support. I truly appreciate the support from my girl friend, Nan Hu, who has been accompanying, and encouraging me during my master study.

TABLE OF CONTENTS

List of Figures

Chapter 2

Chapter 3

Appendix

LIST OF TABLES

CHAPTER 1

Overview

Elucidating the interactions between cellulose and hemicelluloses is of fundamental importance for understanding the molecular architecture of plant cell walls and utilizing these renewable materials.[1] One aim of this study is to quantify the amount of xyloglucan (XG) adsorbed onto cellulose and investigate how cellulose morphology and surface charge affect the adsorption of XG. The interaction of XG with cellulose model surfaces was studied by surface plasmon resonance spectroscopy (SPR), quartz crystal microbalance with dissipation monitoring (QCM-D), and atomic force microscopy (AFM).

The presence of lignin during the enzymatic hydrolysis of cellulose leads to non specific adsorption of cellulase onto lignin,[2-5] which inhibits the effectiveness of cellulase. Non-ionic surfactant can enhance the effectiveness of cellulase.[6-8] Another aim of this study is to better understand the interactions of cellulase with the functional groups of lignin on a molecular basis by monitoring the adsorption of cellulase onto self-assembled monolayers (SAMs). The effects of the non-ionic surfactant Tween 80 on cellulase adsorption is also investigated. The combination of SPR, QCM-D and AFM allows for the monitoring of cellulase adsorption.

This thesis consists of five chapters. Chapter 2 provides an introduction and review related to these studies. It begins with the components and structure of primary plant cell walls. The subsequent discussion includes cellulose, hemicelluloses, and cellulases. Next, some basic knowledge about surfactants is introduced. Finally, analytical techniques including SPR, QCM-D, and AFM are presented.

Chapter 3 describes the adsorption of XG onto three cellulose thin films, an amorphous regenerated cellulose (RC) film, a negatively charged sulfated nanocrystalline cellulose (SNC) film and a non-charged desulfated nanocrystalline cellulose (DNC) film.

Chapter 4 describes the adsorption of XG onto methyl, hydroxyl, and carboxyl-terminated SAMs (SAM-CH_3, SAM-OH and SAM-COOH). The effects of Tween 80 on cellulase adsorption is also discussed.

Finally, Chapter 5 summarizes the overall conclusions of these studies and supplementary experimental results are provided in the appendix.

References

(1) Ragauskas, A. J.; Williams, C. K.; Davison, B. H.; Britovsek, G.; Cairney, J.; Eckert, C. A.; Frederick, W. J., Jr.; Hallett, J. P.; Leak, D. J.; Liotta, C. L.; Mielenz, J. R.; Murphy, R.; Templer, R.; Tschaplinski, T. *Science (Washington, DC, U. S.)* **2006**, *311*, 484.

(2) Berlin, A.; Balakshin, M.; Gilkes, N.; Kadla, J.; Maximenko, V.; Kubo, S.; Saddler, J. *J. Biotechnol.* **2006**, *125*, 198.

(3) Chernoglazov, V. M.; Ermolova, O. V.; Klyosov, A. A. *Enzyme Microb. Technol.* **1988**, *10*, 503.

(4) Tu, M.; Pan, X.; Saddler, J. N. *J. Agric. Food Chem.* **2009**, *57*, 7771.

(5) Yang, B.; Wyman, C. E. *Biotechnol. Bioeng.* **2006**, *94*, 611.

(6) Börjesson, J.; Peterson, R.; Tjerneld, F. *Enzyme Microb. Technol.* **2007**, *40*, 754.

(7) Eriksson, T.; Börjesson, J.; Tjerneld, F. *Enzyme Microb. Technol.* **2002**, *31*, 353.

(8) Sipos, B.; Dienes, D.; Schleicher, Á.; Perazzini, R.; Crestini, C.; Siika-aho, M.; Réczey, K. *Enzyme Microb. Technol.* **2010**, *47*, 84.

CHAPTER 2

Literature review

2.1. Plant cell walls

2.1.1. Components of plant cell walls

Plant cell walls constitute the most abundant biomass and provide materials for textiles, paper and other products.[1-2] Today, plant cell walls are also considered a promising source for renewable and sustainable energy, for example through the conversion of lignocellulosic biomass to fermentable sugars and fermentation to biofuels.[3] Plant cell walls include primary cell walls and secondary cell walls. Primary cell walls are deposited during cell growth; they are mechanically stable while extensible enough to allow cell expansion.[1] Primary walls not only define the size and shape of plant cells but greatly impact their growth rate.[4] Secondary cell walls, which are much thicker than primary cell walls, are deposited on the inside of the primary wall when the cell stops growing and provide mechanical stability to the mature cell.[1]

The major components of primary cell walls include cellulose, hemicelluloses, pectins, and proteins.[5] Secondary cell walls mainly contain cellulose, hemicelluloses, lignins, and proteins.[6] The average cellulose content of wood is 43 ± 2% by weight for both hardwood and softwood.[1] Hemicelluloses account for 20 to 35% of the weight of hardwoods, versus as much as 30% of the weight of softwoods.[7] The lignin contents of hardwoods range from 18 to 25% by weight, whereas they range from 25 to 35% by weight in softwoods.[8]

2.1.2. Primary plant cell wall structure

The primary cell wall structure has been widely studied. In 1973, Keegstra *et al.* proposed the first complete model for the structure of primary cell walls.[9] In this model, cellulose microfibrils are coated with xyloglucan chains and bridged by pectic polysaccharides, forming a vast macromolecular network. The matrix polymers, such as xyloglucan and pectic polysaccharides, are covalently linked, but xyloglucan is bound to cellulose *via* hydrogen bonds. However, because there was no concrete evidence supporting covalent linkages between pectin and xyloglucan in the model of Keegstra *et al.*, Hayashi and Fry came up with another model, which became more popular.[10-12] This model hypothesizes that in primary cell walls there is more xyloglucan than is required to coat all cellulose microfibrils with a monolayer and that xyloglucan molecules are long enough to bind to two or more microfibrils at the same time through hydrogen bonds thus forming a network. The xyloglucan network spanned adjacent microfibrils and prevents the re-orientation of microfibrils; it also offers flexibility to the primary cell walls by helping microfibrils to slide during cell growth. Pectic polysaccharides and structural proteins form another independent network that is entangled with the cellulose–xyloglucan network through non-covalent bonds. Other structural models were also proposed. Talbott and Peter, for example, agreed with Hayashi and Fry that xyloglucan coats and tethers the cellulose microfibrils, but they considered pectic polymers as a second layer coating the microfibrils above the xyloglucan coat.[13] A free portion of xyloglucan chains is embedded in the gel like pectin phase and interacts with pectic polymers *via* weak intermolecular forces. The pectin network is separated from, but coextensive with the xyloglucan–cellulose network. Ha and colleagues employed a nuclear magnetic resonance technique to study the primary wall structure of onion cells.[14] They assumed that the wall consists of three to four stacked layers of cellulose

microfibrils, with the cellulose layers being about 20 nm apart from each other. Xyloglucan tethers the microfibrils within each layer but not between layers and the pectic gel serves as a spacer between the cellulose–xyloglucan layers. Mechanical strength in directions parallel to the cell surface is controlled by the microfibril layers, whereas wall thickness and mechanical properties across the cell wall are controlled by the pectic layers. Schematic illustrations of the four models described above, generated by Cosgrove, are shown in Figure 2.1.[15] In 2011, Dick-Perez *et al* proposed a new model for the primary cell wall, using solid-state NMR.[16] In this model limited amounts of xyloglucan intercalated into the cellulose microfibrils rather than coating cellulose microfibrils on the surface, however, pectin had extensive interactions with both cellulose and xyloglucan and it plays a critical role in maintaining the structure and function of the primary plant cell wall. All three of these polysaccharides integrate into a single network, which serves as the load bearing structure in the primary plant cell wall. A schematic representation of this model is shown in Figure 2.2.[16]

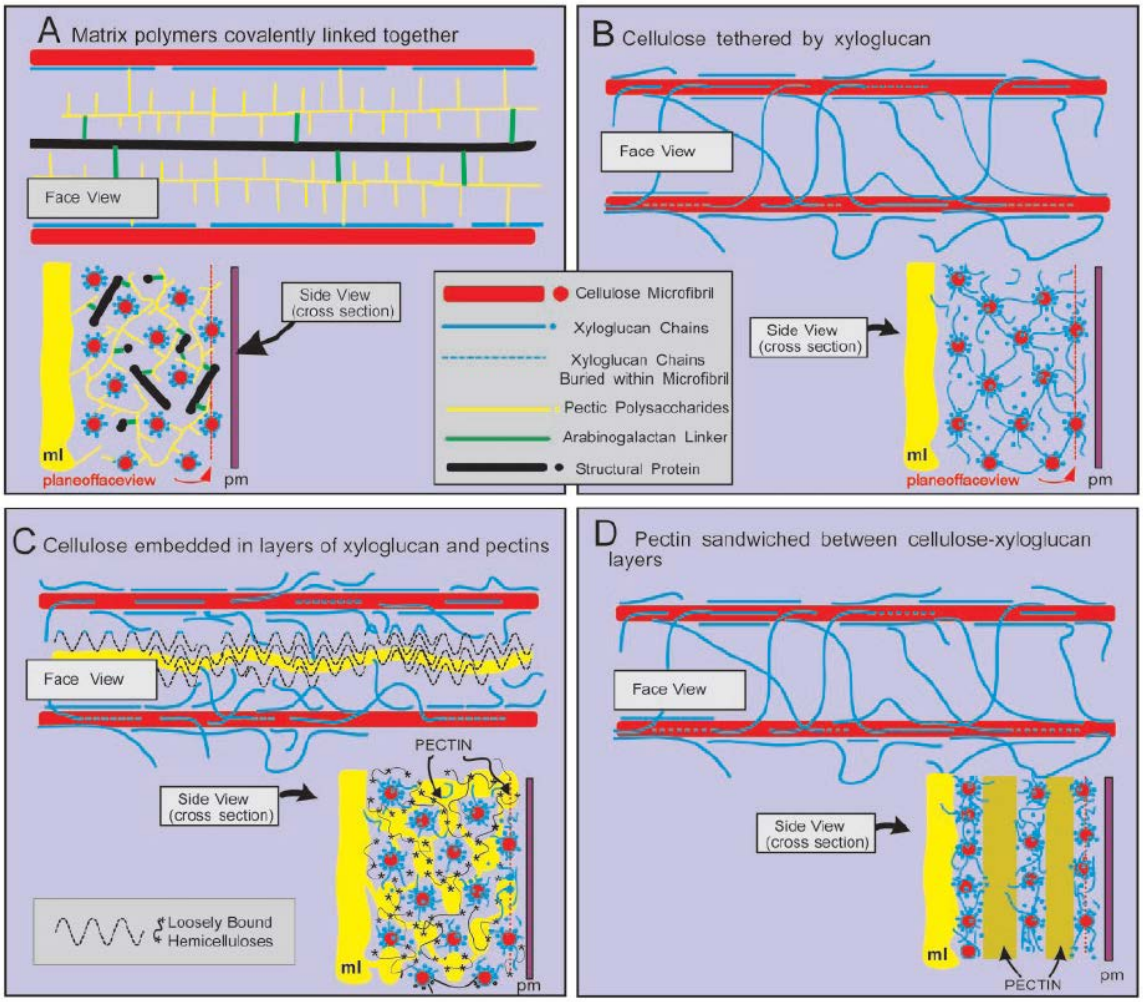

Figure 2.1. Models of primary cell wall structure. A, The model of Keegstra *et al.*[9] B, The "tethered network" model of Hayashi and Fry.[10,17] C, The model of Talbott and Peter.[13] D, The model of Ha *et al.*[14] (Reprinted from ref 15; fair use; Copyright 2001 American Society of Plant Physiologists)

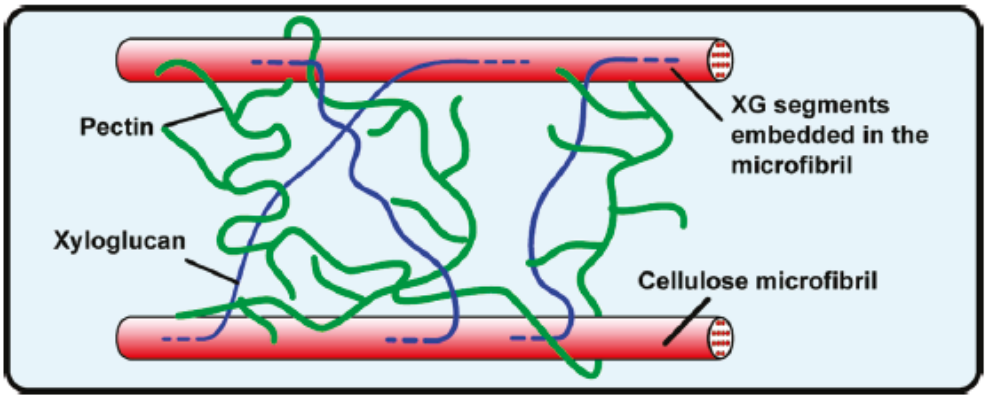

Figure 2.2. Model of primary cell wall structure by Dick-Perez *et al.*[16] (Reprinted from ref 16; fair use; Copyright 2011 American Chemical Society)

2.2. Cellulose

2.2.1. Cellulose molecular structure

Cellulose is the dominant component in plants and serves to maintain their structure. It is also produced by bacterial, fungal, and algal species and found even in some animals.[8] The polymeric nature of cellulose was first elucidated by Staudinger in the 1920s.[18] The molecular structure of cellulose is shown in Figure 2.3. Anhydroglucose units (AGUs) are covalently linked by β-(1-4) glucosidic bonds and extend to form a linear polymer chain with three hydroxyl groups per AGU. The chain length of cellulose is expressed by the number of AGUs, which varies with the source of the material.[19] Every other AGU is rotated 180° in plane to preserve the preferred angle of the acetal oxygen bridge so that the repeating unit of cellulose is composed of two adjacent AGUs (cellobiose). Being thermodynamically favorable, all pyranose rings adopt a $^4C_1$ conformation in which all hydroxyl groups are in equatorial positions. The cellulose chain has two different ends, the non-reducing end contains a D-glucose unit with an original C4-OH

group, whereas the reducing end is terminated with an original C1-OH group, as shown in Figure 2.3.

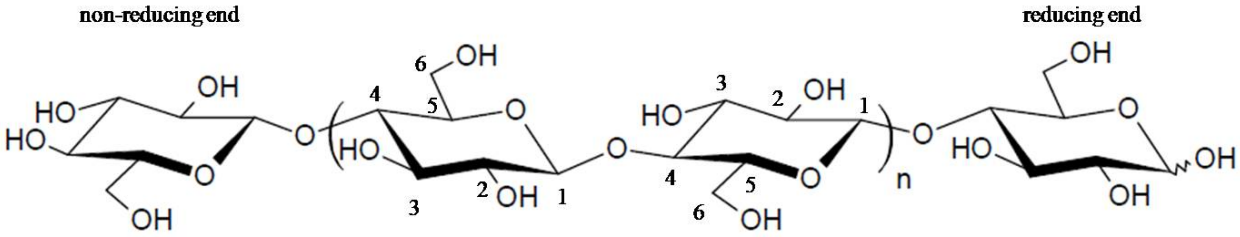

Figure 2.3. Cellulose molecular structure.

2.2.2. Cellulose crystal structure

Cellulose tends to crystallize because of hydrogen bonds and van der Waals interactions.[20] Four principle polymorphs of cellulose are known, named cellulose I, II, III, and IV. Cellulose I can be converted to the thermodynamically more stable cellulose II by mercerization with aqueous sodium hydroxide or by regeneration, which is done by dissolution of cellulose I in a solvent, followed by reprecipitation. Cellulose III is reversibly formed when celluloses I and II are treated with liquid ammonia. Cellulose IV can be prepared by heating cellulose III in glycerol. The interconversions of the four principle cellulose polymorphs are shown in Figure 2.4.[21]

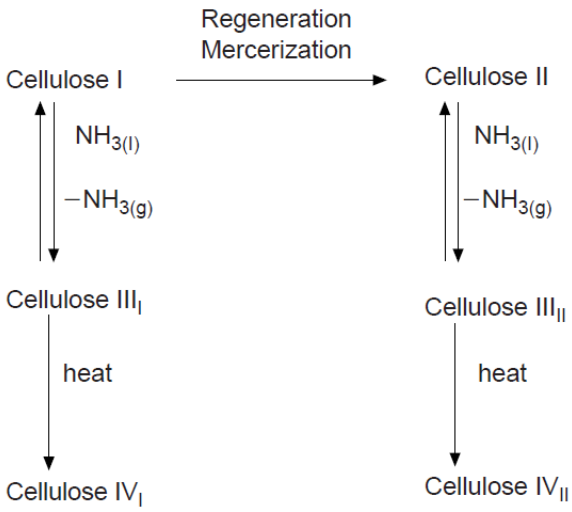

Figure 2.4. Interconversions of cellulose crystal polymorphs. (Reprinted from ref 21; fair use; Copyright 1997 Blackie Academic & Professional)

Native cellulose has the crystalline form of cellulose I, which is also the most extensively studied form.[19,21-23] In the 1980s, it was discovered that cellulose I contains two distinct crystalline phases, namely cellulose I_α and I_β.[24] On the basis of the work of Nishiyama *et al.*,[25] Jarvis compared the crystal structures of these two forms and illustrated the packing of the cellulose chains into sheets and the stacking of these sheets into microfibrils (Figure 2.5).[23] In cellulose I_α, the conformations of adjacent glucose units in a cellulose chain, shaded grey and yellow in Figure 2.5 (a), differ slightly, but all cellulose chains are equivalent. In cellulose I_β (Figure 2.5 (b)), the conformations of glucose units within the same sheet are identical, but adjacent sheets contain two kinds of chains that differ in their conformation. Cellulose chains that pass through the origin of the unit cell are shaded yellow and those passing through the center of the unit cell are shaded grey. The different cellulose chain conformations result in distinct hydrogen bond patterns in cellulose I_α and I_β.

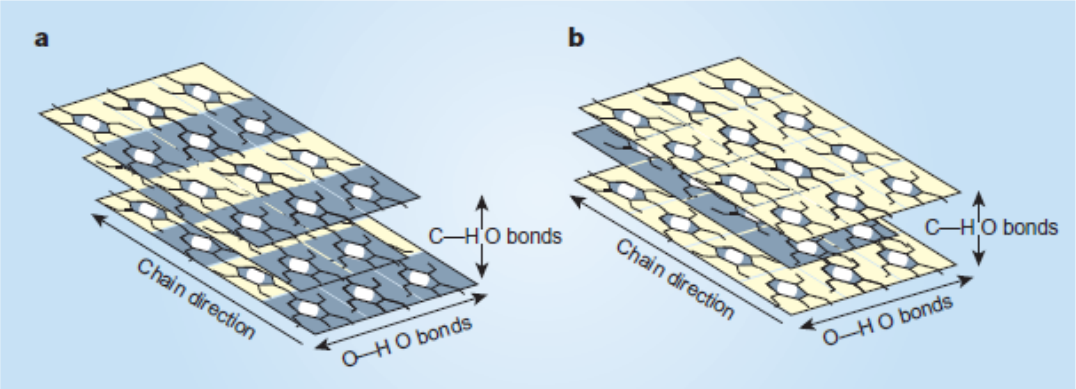

Figure 2.5. Cellulose chain arrangement in (a) cellulose I_α and (b) cellulose I_β. (Reprinted from ref 23; fair use; Copyright 2003 Nature Publishing Group)

2.2.3. Cellulose nanocrystals

As an emerging renewable nanomaterial, cellulose nanocrystals (CNCs) show promise in many applications, such as food, pharmaceuticals, paper and composite manufacturing. The main advantages of CNCs include extreme abundance, relatively low cost, high strength and stiffness, and high specific surface area.[26]

Acid hydrolysis is the main method for the extraction of CNCs from cellulose microfibrils. The amorphous regions of the microfibrils are removed by concentrated acid, whereas the crystalline regions have a higher resistance to acid hydrolysis and remain intact. The acid hydrolysis product is diluted with water for termination of the hydrolysis reaction and dialyzed against DI water for removal of the acid. Additional steps in the preparation of CNCs include filtration, sonication, and centrifugation. The properties of CNCs depend on various factors, such as the cellulose source, nature of the acid, hydrolysis time, temperature, and acid to cellulose ratio. For example, CNCs prepared with hydrochloric acid are weakly charged, and the low surface charge limits the colloidal stability of their suspensions. As a result, CNCs prepared

with hydrochloric acid tend to flocculate.[27] However, if sulfuric acid is used as hydrolyzing agent, negatively charged sulfate groups are introduced on the CNC surface, and the resulting strong electrostatic repulsion between CNCs promotes their dispersion in aqueous systems. The geometrical dimensions of CNCs also vary widely, depending on the source of cellulose and the CNC preparation conditions.[28] Precise morphological measurements are carried out by microscopy or scattering techniques (including light scattering and neutron scattering). Peng *et al.* summarized some reported CNC dimensions, as shown in Table 2.1.[26]

Table 2.1. Reported lengths (*L*) and diameters (*d*) of CNCs from various cellulose sources[29-37]

Source	*L* (nm)	*d* (nm)	Aspect ratio (*L*/*d*)	Technique	References
Bacterial	100-1000	10-50	2-100	TEM	28
Cotton	100-150	5-10	10-30	TEM	28
	150-210	5-11	15-42	E-SEM	34
Microcrystalline cellulose	~500	10	50	AFM	35
Ramie	50-150	5-10	5-30	TEM	30
Sisal	100-500	3-5	20-167	TEM	32
Tunicate	1160	16	73	DDLS	31
	100-several 1000	15-30	3-67	TEM	33
Valonia	> 1000	10-20	50-100	TEM	36
Wood	100-300	3-5	20-100	AFM	29

Perhaps the most interesting property of sulfuric acid-treated CNCs is their ability to form a colloidal liquid-crystalline chiral nematic phase.[38] In dilute suspensions, CNCs are randomly oriented. However, when water is gradually removed from a dilute CNC suspension, a critical concentration is reached, at which the suspension spontaneously separates into an upper isotropic phase and a lower anisotropic liquid-crystalline phase. In the liquid crystalline phase, the rod-like CNC within one horizontal plane align along a certain vector. The direction of this vector rotates slightly about the normal of the plane with respect to the direction of the vector of the adjacent plane. The stacked planes form the chiral nematic structure, as shown in Figure 2.6.[28] This self-ordering phenomenon of CNC suspensions is driven by entropy. CNCs tend to adopt certain orientations to minimize excluded volume effects, resulting in higher packing

entropy.[28] The critical concentration of an electrolyte-free aqueous CNC suspension mainly depends on the charge density of the particles and their geometric axial ratio.[39] The equilibrium between isotropic phase and liquid crystalline phase is sensitive to the presence of electrolytes and the nature of electrolyte counterions. A self-ordering phenomenon has also been observed when CNC suspensions were exposed to external magnetic or electric fields.[40] When water is completely removed from the suspension, the chiral nematic structure may be preserved in solid iridescent CNC films, which have many potential applications, including decorative materials and security paper.[28]

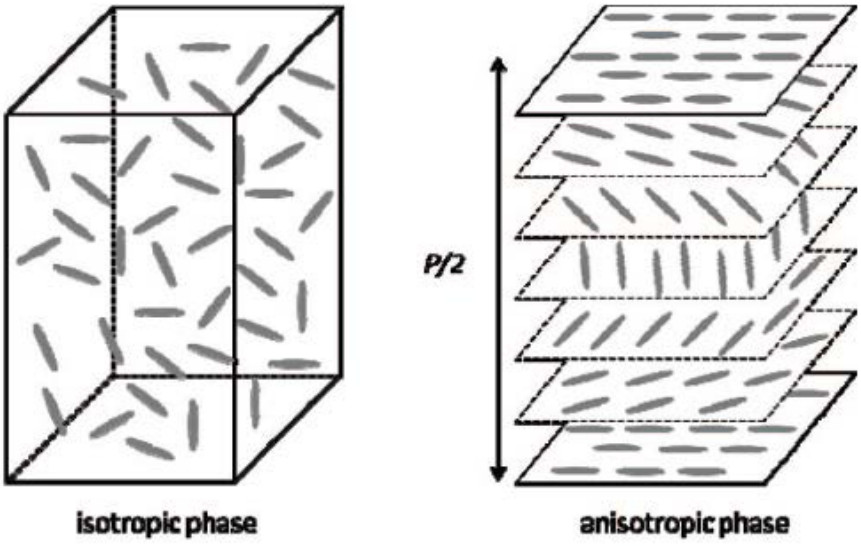

Figure 2.6. Orientation of CNCs in isotropic and chiral nematic colloidal phases. (Reprinted from ref 28; fair use; Copyright 2010 American Chemical Society)

CNCs have been widely studied as reinforcing agents in polymeric matrices for nanocomposite development. In 1995, Favier *et al.* first reported the physical incorporation of CNCs derived from tunicates as reinforcing filler in a poly(styrene-co-butyl acrylate) matrix,

resulting in nanocomposite films with substantially enhanced mechanical properties.[41] The enhanced properties of this novel nanocomposite was ascribed to a hydrogen-bonded percolation network of CNCs within the polymer matrix. CNCs were also incorporated into other polymer matrices, such as poly(caprolactone),[42-43] poly(oxyethylene),[44-46] cellulose acetate butyrate,[47-48] carboxymethyl cellulose,[49] and poly(vinyl chloride).[50-52] Parameters that affect the mechanical properties of CNC-polymer nanocomposites include the aspect ratio and surface characteristics of the CNC, the processing techniques, and moisture.[53] Due to the hydrophobic properties of most thermoplastics and the hydrophilic nature of CNCs, currently the main challenge in the development of CNC nanocomposites is the effective dispersion of CNCs in the polymer matrix. Another limitation of CNCs is the low degradation temperature (about 230 °C), so that only thermoplastics with processing temperatures below 200 °C can be used.[39]

CNCs are also attracting increasing attention in biomedical applications. Several studies have been done to assess CNC toxicity.[54-55] Although the results of these studies showed that CNCs do not pose serious safety concerns, further testing is necessary to assess their toxicity in different environments. In 2007, Dong and Roman reported labeling of CNCs with fluorescein-5'-isothiocyanate for fluorescence bioassay and bioimaging applications.[56] CNCs are also considered good candidates as drug delivery vehicles.[54]

2.2.4. Cellulose model substrates

The methodology of preparing ultrathin cellulose films is fairly new; most methods emerged in the early 1990s[57]. Recently, cellulose model substrates are gaining more research interest because of their utility in the determination of the adsorption of polyelectrolytes, surfactants, and enzymes onto cellulose, the measurement of interactions between cellulose and other materials, and the investigation of cellulose swelling.[22] Currently there are two reliable

methods for the preparation of smooth cellulose model surfaces: Langmuir-Blodgett (LB) deposition[58] and spin coating.[59]

Schaub *et al.* were the first to report the use of the LB-technique to obtain trimethylsilyl cellulose (TMSC) multilayers on silicon wafers and subsequent exposure of the TMSC LB-films to the vapor of an aqueous HCl solution, leading to cleavage of the trimethylsilyl groups and *in-situ* conversion of the TMSC films to ultrathin cellulose films.[60] An alternative technique for obtaining cellulose thin films is spin coating. Gunnars *et al.* dissolved cellulose in *N*-methylmorpholine-*N*-oxide (NMMO)/dimethyl sulfoxide (DMSO) and spin coated the cellulose solution on polymer-treated silicon oxide wafers.[61] Cellulose model thin films were obtained with thicknesses in the range of 20-270 nm, controlled by the relative amount of DMSO in the solvent system.[61-62] Kontturi *et al.* refined the method of Gunnars *et al.* by directly depositing TMSC onto untreated silicon substrates by spin coating and subsequently exposing the TMSC films to HCl vapor.[63] The thickness of the resulting cellulose film was around 20 nm, with a maximum surface roughness of 3 nm. In this method, the roughness of the film is greatly influenced by the spin coating conditions, TMSC concentration, nature of the substrate, and solvent. Edgar and Gray developed a method for the preparation of smooth model surfaces of crystalline cellulose I, in which an aqueous cellulose I nanocrystal suspension is spin coated onto a freshly cleaved mica surface.[64-65]

Compared to LB deposition, spin coating provides a faster method, but the roughness of the film may increase with film thickness. For example, if the concentration of the TMSC solution is doubled from 10 to 20 g/L, the thickness of the film increases from 20 to 50 nm and the roughness increases from 2 to 10 nm.[66] In contrast, with the LB-technique, the thickness of the films is controlled by the number of layers deposited and the film roughness is independent

of film thickness.[22] The main drawback of the LB-technique is its requirement for special equipment, like a Langmuir trough and a computer controlled thermostat.[66]

2.3. Hemicelluloses

Hemicelluloses account for up to 50% of the biomass of annual and perennial plants.[67] Four general types of hemicelluloses are xylans, mannans, β-glucans with mixed linkages, and xyloglucans. The specific structure of hemicelluloses varies widely, depending on species and cell types.[67-68]

As opposed to cellulose, hemicelluloses are heteropolysaccharides containing various sugars. The principle sugars are D-xylose, L-arabinose, D-glucose, D-galactose, D-mannose, D-glucuronic acid, 4-*O*-methyl-D-glucuronic acid, and D-galacturonic acid.[69] Hemicelluloses have very low degrees of polymerization in contrast to cellulose, ranging from 80 to 200.[70-71] Hemicellulose chains are mostly branched, exist in an amorphous form, and are generally very soluble in water.[72]

Hemicelluloses strengthen plant cell walls by interacting with cellulose and lignin. Isolated hemicelluloses and their derivatives are employed in industry as food additives, thickeners, emulsifiers, and adsorbents.[72]

2.4. Cellulases

2.4.1. Classification of cellulases

Cellulases are enzymes produced by microorganisms that can degrade β-D-glucans.[73] Cellulases are usually classified on the basis of their enzymatic action and can be divided into (1) endoglucanases (EG) or 1,4-β-D-glucanohydrolases, (2) exoglucanases, including 1,4-β-D-

glucanglucanohydrolases and 1,4-β-D-glucancellobiohydrolases, and (3) β-glucosidases or β-glucoside glucohydrolases. Endoglucanases attack the amorphous part of cellulose microfibrils and cleave bonds along cellulose chains, which results in new chain ends and a rapid decrease in the degree of polymerization of cellulose.[74-75] Exoglucanases, also known as cellobiohydrolases, are processive enzymes that act at the ends of cellulose chains.[76-78] Exoglucanases can also act on the crystalline part of cellulose, producing glucose and cellobiose and slowly decreasing the degree of polymerization of cellulose.[79] β-glucosidases hydrolyze cellobiose into glucose.[80] Compared to other glycoside hydrolases, cellulases have a unique ability to cleave β-1,4-glucosidic bonds between glucosyl residues. A schematic illustration of the enzymatic hydrolysis of cellulases is shown in Figure 2.7.[80]

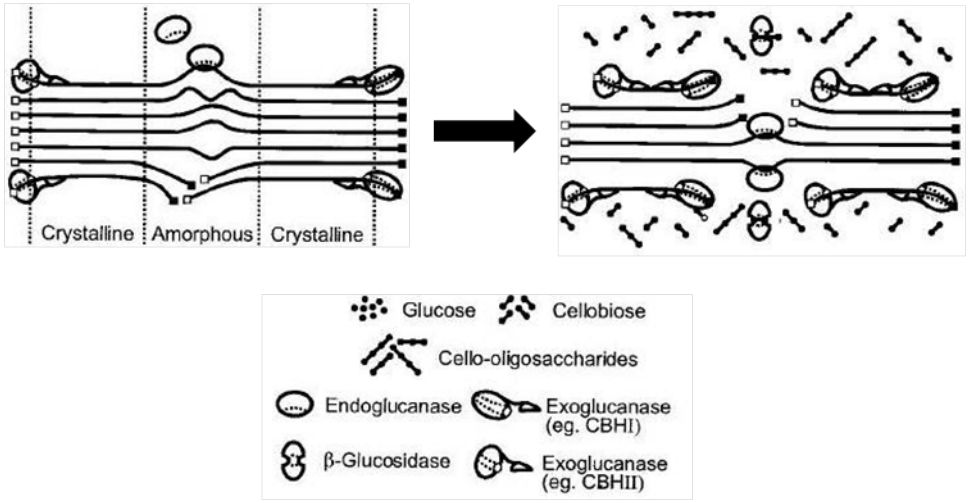

Figure 2.7. Schematic representation of the hydrolysis of a cellulose microfibril by a non-complexed cellulase system. (Redrawn from ref 80; fair use; Copyright 2002, American Society for Microbiology)

In 1991, Stahlberg *et al.* first reported the two domain structure model of cellulases after studying the adsorption of *Trichoderma reesei* cellobiohydrolase I to microcrystalline cellulose. The model structure developed by Stahlberg *et al.* contains a distinct catalytic domain and a binding domain.[81] Further research revealed the role of the cellulose binding domain (CBD) in cellulose hydrolysis: it brings the catalytic domain close to the substrate and promotes the release of cellulose fragments from crystalline cellulose. The presence of the CBD is of particular importance for the processivity of exoglucanases.[82]

2.4.2. Non-complex and complex cellulase systems

Cellulase systems can be divided into two categories: non-complex (non-aggregating) and complex (aggregating) systems based on the hydrolyzing approaches adopted by the microorganisms.[83-84]Aerobic fungi and bacteria are able to penetrate cellulosic substrates and

produce non-complex cellulase systems within confined cavities of cellulose particles. The enzymes do not form high-molecular-weight complexes. In contrast, anaerobic microorganisms typically generate complex cellulase systems because of their inability to effectively penetrate cellulosic materials. In this case, stable enzymes containing high-molecular-weight protein complexes are developed as an alternative means to degrade cellulose.[80,83-84]

The non-complex cellulase system of *T. reesei* (initially called *Trichoderma viride*) has been widely studied since the 1950s.[85] *T. reesei* produces at least two exoglucanases (CBHI and CBHII), five endoglucanases (EGI, EGII, EGIII, EGIV, and EGV), and two β-glucosidases (BGLI and BGLII).[86-87] The relative amounts of CBHI and CBHII in the total cellulolytic protein mixture are 60% and 20% by mass, respectively, accounting for most of the cellulase activity. CBHI and CBHII can even hydrolyze, although slowly, cellulose nanocrystals without endoglucanases.[88] Both CBHI and CBHII have tunnel-shaped active sites enclosed by two (CBHI) or four (CBHII) surface loops. Single glucose chains bind to the active sites inside the tunnels in defined orientation *via* protein–sugar interactions. It is thought that one end of a glucose chain is fed into the tunnel and moves through the entire tunnel followed by the rest of the molecule. Cellobiose, the major product of the hydrolysis, is cleaved off of the cellulose molecule at the active site and released from the other end of the tunnel. Generally, CBHI acts at the reducing end of a cellulose chain whereas CBHII acts at the non-reducing end.[79-80]

2.4.3. Adsorption of cellulase onto lignocellulosic materials

Understanding the mechanism of cellulase adsorption onto lignocellulosic materials is critical for optimizing the enzymatic cellulose hydrolysis process. CBDs bind to cellulosic substrates by non-covalent interactions. Compared to the hydrolysis process, cellulase adsorption is rapid and reaches an equilibrium in a short time.[80] The Langmuir isotherm is commonly used

to describe cellulase adsorption, provided that it can be described by one single adsorption equilibrium constant and a specific adsorption capacity. The Langmuir isotherm is expressed as:

$$E_a = \frac{W_{\max} K_P E_f}{1 + K_P E_f}$$

where E_a is adsorbed cellulase, W_{max} is maximum cellulase adsorption, E_f is free cellulase, and K_p is the dissociation constant. The Langmuir model represents a simple mechanistic model and it fits the data well in most cases. But the Langmuir model may not apply in situations that involve partially irreversible cellulase adsorption,[89] interaction among cellulase components at high concentrations,[90] and multilayer adsorption.[91] Other equilibrium models have been developed to describe the situations above, including two-site adsorption models,[92-93] Freundlich isotherms,[93] and combined Langmuir–Freundlich isotherms.[93]

2.5. Surfactants

2.5.1. Molecular structure of surfactants

Surfactants, or surface-active agents, are important ingredients in a large number of formulations and processes, such as ore flotation, paint technology, lubrication, paper making, and oil recovery.[94-95] Surfactant molecules generally have a hydrophilic group, which has strong attraction for the solvent, and a hydrophobic group, which has very little attraction for the generally aqueous solvent. The hydrophobic group is usually a hydrocarbon chain, and the hydrophilic group is an ionic or highly polar group. According to the nature of the polar group, surfactants can be classified into three classes: cationic, anionic and non-ionic.[94,96]

1. Cationic surfactants: The surface active portion of the molecule carries a positive charge, as in $(C_{16}H_{33})N^{+}(CH_3)_3Br^{-}$.

2. Anionic surfactants: The surface active portion of the molecule bears a negative charge, as in $CH_3(CH_2)_{11}OSO_3^-Na^+$ (sodium dodecyl sulfate or SDS).
3. Non-ionic surfactants: The surface active molecule bears no charge in the predominant working range of pH,[94] for example Polysorbate 80 (Tween 80), as shown in Figure 2.8.

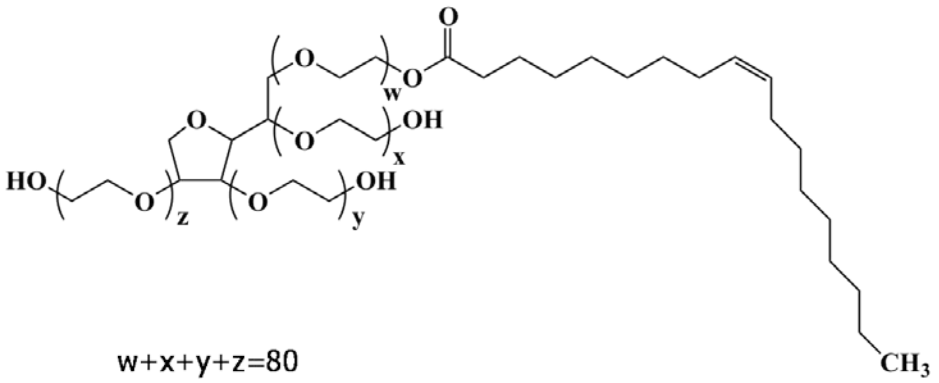

Figure 2.8. Chemical structure of non-ionic surfactant Tween 80.

2.5.2. Adsorption of non-ionic surfactants at solid–liquid interfaces

2.5.2.1. Adsorption of non-ionic surfactants on hydrophilic solids

Reversible adsorption onto hydrophilic or polar solids is observed when the concentration of non-ionic surfactants is below or around their critical micelle concentration (CMC). In this case, adsorption isotherms reach a plateau around the CMC, and the plateau decreases as the polar chain length increases.[97-99] For very short polar chains, step isotherms are obtained. In contrast, for long polar chains, the adsorption isotherms have the shape of Langmuir isotherms and do not show clear inflection points. When the polar chain length is of intermediate length, typical sigmoidal shape isotherms are observed. Fluorescence spectroscopy,[98,100-101] neutron reflectometry,[102] and atomic force microscopy[103-104] experiments have revealed that adsorption involves strong lateral interactions between surfactant molecules and weak interactions with the

solid surface. Adsorbed molecules may form flattened micelles and further extend to bilayer structure.

2.5.2.2. Adsorption of non-ionic surfactants on hydrophobic solids

The adsorption of non-ionic surfactants onto hydrophobic solids has also been investigated.[105-106] Adsorption isotherms leveled off well below the CMC.[95] The self-consistent field theory is often employed to describe the non-ionic surfactant adsorption.[107-108] Surfactants tend to form lower curvature aggregates on hydrophobic solids. This behavior can be explained by the fact that a lower free energy of the hydrophobic solid is achieved when the contact between hydrophobic substrate and water is minimized.

2.6. Self-assembled monolayers (SAMs)

Self-assembled monolayers (SAMs) are highly ordered and oriented organic molecule assemblies on a solid surface.[109-110] Molecules that form SAMs have a chemical functionality, with high affinity to a specific substrate, thus they adsorb spontaneously from solution or the gas phase onto solid surfaces to form SAMs.[109] SAMs provide a flexible and simple system which is frequently employed to tailor the surface properties. The most extensively studied SAM is prepared from the adsorption of alkanethiols onto thin gold films,[111-116] as shown in Figure 2.9. Gold is a good choice as a substrate because gold thin films are easy to obtain using techniques such as vapor deposition and electrodeposition, and gold is an inert metal which does not react with most chemicals. The most common method of preparing SAMs on gold is to immerse freshly cleaned gold substrates into dilute thiol solution (alkanethiols dissolved in ethanol with concentrations from 1 to 10 mM) for 12 to 18 hours at room temperature.[109] It is believed an

oxidative addition reaction occurs between the S-H and the gold substrates, resulting in the release of H_2 molecules, as shown in Figure 2.10. As reported in the literature,[117] 80-90% of the alkanethiol molecules in the finally formed SAM adsorb onto the gold substrate in the first few minutes, which can be well described by Langmuir adsorption. In the subsequent hours the adsorbed alkanethiol molecules adjust their confirmation to crystallize.

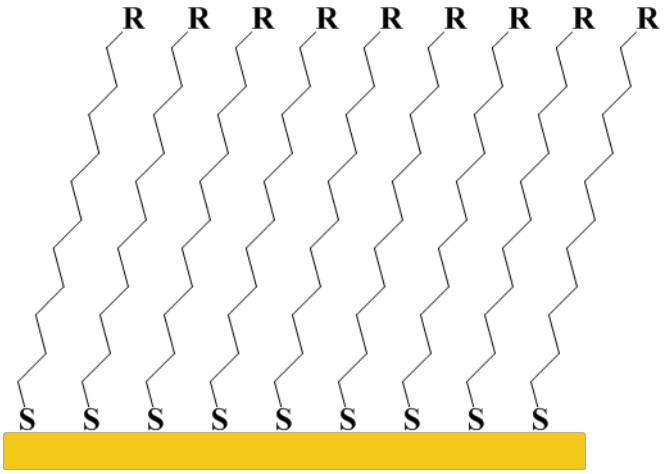

Figure 2.9. Schematic representation of the SAM. S refers to sulfur in the alkane thiol and R indicates the terminal functional group of the SAM.

$$R - SH + Au_n^0 \rightarrow R - S^- Au^+ Au_{n-1}^0 + 1/2H_2(g)$$

Figure 2.10. Reaction between alkyl thiol and gold.

2.7. Analytical techniques

2.7.1. Surface plasmon resonance spectroscopy

The surface plasmon resonance (SPR) technique employs an optical method to monitor the real time refractive index change within the vicinity (~ 200 nm) of a sensor surface.[118] In SPR experiments, the interactions between the analyte in solution and binding sites immobilized on the sensor surface result in a refractive index change near the sensor surface, providing detailed information on binding kinetics and binding affinity for the interaction.[119]

The most frequently used geometry for SPR refractometers is the Kretschmann prism configuration, as shown in Figure 2.11.,[120] which integrates p-polarized light, a glass prism coated with a thin metal film, and a photodiode as a light detector.[121] SPR is a technique based on total internal reflection. A monochromatic, p-polarized light beam is generated by a light source and travels from glass, an optically dense medium, towards an optically less dense ambient medium. When the incident angle θ is larger than a critical angle θ_c, total internal reflection occurs. Most of the light is reflected without significant leaking to the surroundings. However, a component of the incident light (evanescent wave or field) can penetrate the metal film if it is thin enough. This evanescent field propagates along the interface between the metal and the ambient medium and couples with the free oscillating electrons in the metal film to excite surface plasmon.[122]

The critical angle θ_c, can be determined from Snell's law[123]

$$n_1 \sin\theta_1 = n_2 \sin\theta_2 \qquad [2.1]$$

where $n_1$is the refractive index of medium 1 and n_2 is the refractive index of medium 2, θ_1 is the incident angle and θ_2 is the refractive angle. Figure 2.12 illustrates the relation between θ_1 and θ_2.

When θ_1 increases to θ_c, total internal reflection occurs and θ_2= 90°. In that case, Snell's law can be rearranged as[123]

$$\sin\theta_c = \frac{n_2}{n_1} \qquad [2.2]$$

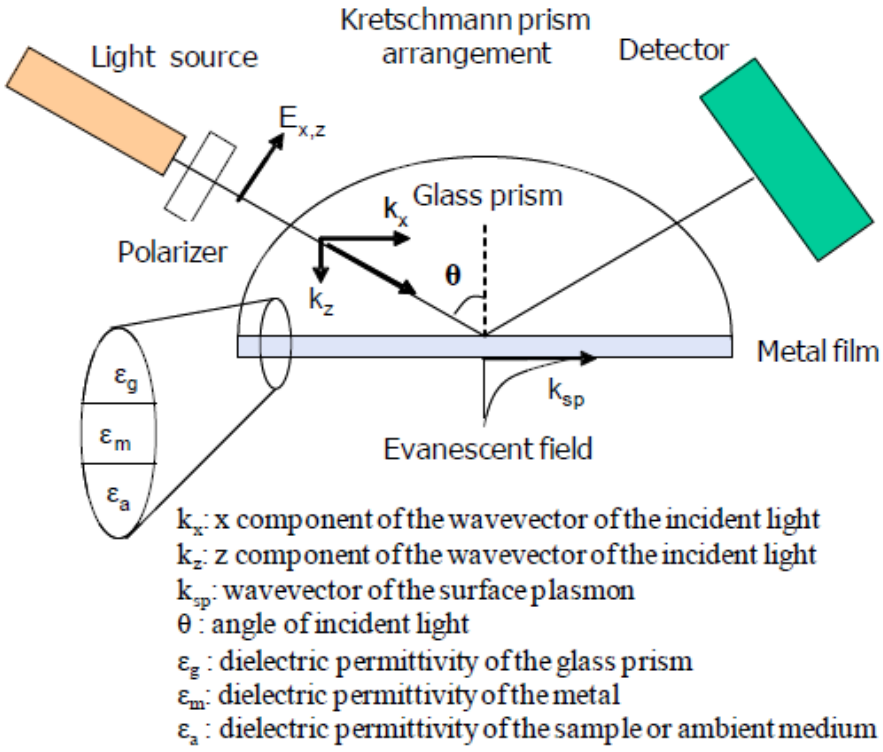

Figure 2.11. Kretschmann prism configuration. (Reprinted from ref 120; fair use; Copyright 2010 Liu Z)

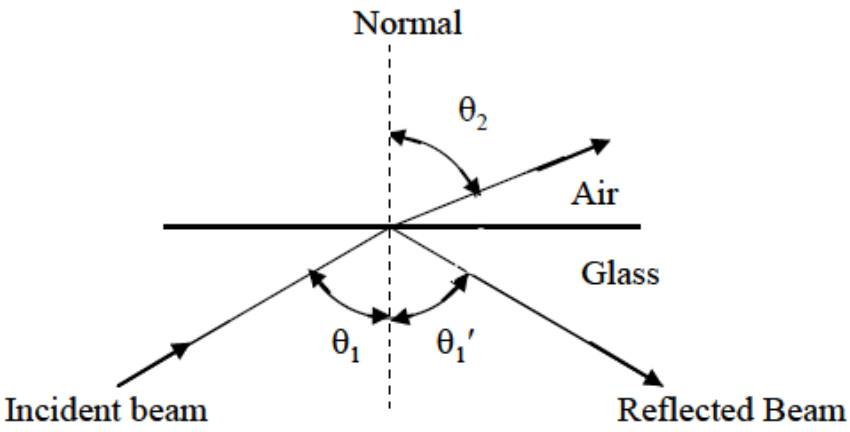

Figure 2.12. Schematic illustration of Snell's law. (Reprinted from ref 120; fair use; Copyright 2010 Liu Z)

The surface plasmon propagates along the interface between the metal and the ambient medium. The wave factor k_{sp} is described as

$$k_{sp} = \frac{2\pi}{\lambda}\sqrt{\frac{\varepsilon_m \varepsilon_a}{\varepsilon_m + \varepsilon_a}} \qquad [2.3]$$

where λ is the wavelength of the incidence light, ε_m is the dielectric permittivity of the metal, and ε_a is the dielectric permittivity of the ambient medium.[124] The propagation vector of the incident light propagating through the glass prism, k, is given by

$$k = \frac{2\pi}{\lambda}\sqrt{\varepsilon_g} \qquad [2.4]$$

where ε_g is the dielectric permittivity of glass prism. The surface-parallel component of the incident propagation vector, k_x is described by

$$k_x = k \cdot \sin\theta = \frac{2\pi}{\lambda}\sqrt{\varepsilon_g} \cdot \sin\theta \qquad [2.5]$$

Setting $\sqrt{\varepsilon}$ = n (refractive index) in eq 2.5 for a non-polar insulator gives

$$k_x = \frac{2\pi}{\lambda} n \cdot \sin\theta \qquad [2.6]$$

In SPR experiments, the incident angle θ is varied until $k_x = k_{sp}$. At this condition, θ is defined as SPR angle θ_{sp}. Combining eqs 2.3 and 2.6, we obtain

$$n_g \cdot \sin\theta_{sp} = \sqrt{\frac{n_m^2 n_a^2}{n_m^2 + n_a^2}} \qquad [7]$$

where n_g, n_m, and n_a are the refractive indices of glass, metal, and the ambient medium, respectively.

SPR detects the intensity of the reflected light as a function of the incident angle. When θ equals θ_{sp} and satisfies eq 2.7, the incident light is transferred to the surface plasmon and only a minimum of reflected intensity is detected. Because the refractive indices of the glass prism, light source, and metal do not change during the experiment, θ_{sp} is only a function of the refractive index of the ambient medium, n_a. Thus, adsorption of analyte onto the metal surface will change the refractive index of the ambient medium, resulting in a change of the resonant angle θ_{sp}.

The change in refractive index between the adsorbed layer and the ambient medium, Δn_a, can be used to determine the surface concentration of adsorbed analyte, Γ, by an equation developed by Feijter *et al*.[125]

$$\Gamma = \frac{L\Delta n_a}{(dn/dc)} \qquad [2.8]$$

where L is the thickness of the adsorbed layer, (dn/dc) is the refractive index increment of the analyte, which can be expressed as

$$\left(\frac{dn}{dc}\right) = \left(\frac{dn}{d\theta_{sp}}\right)\left(\frac{d\theta_{sp}}{dc}\right) \qquad [2.9]$$

where ($dn/d\theta_{sp}$) is obtained by calibration of the SPR instrument with refractive index standards, and ($d\theta_{sp}/dc$) is the change in resonant angle with bulk analyte concentration. The thickness of adsorbed layer, L, is given by

$$L = \Delta\theta_a \left(\frac{dL}{d\theta} \right) \quad [2.10]$$

The value of $\Delta\theta_a$ in eq 2.10 needs to be corrected for the bulk contribution to refractive index change[126]

$$\Delta\theta_a = \Delta\theta_{sp} - c\left(\frac{d\theta_{sp}}{dc} \right) \quad [2.11]$$

By combining the eqs 2.9, 2.10, and 2.11, the surface concentration Γ can be expressed as

$$\Gamma = \Delta\theta_a \left(\frac{dL}{d\theta} \right) \Delta n \left(\frac{dc}{d\theta_{sp}} \right) \left(\frac{d\theta_{sp}}{dn} \right) \quad [2.12]$$

2.7.2. Quartz crystal microbalance with dissipation monitoring

Quartz crystal microbalance with dissipation monitoring (QCM-D) is widely used in the areas of materials science, biophysics, and environmental and clinical analysis. It is a powerful technique for monitoring mass changes during adsorption at solid/air and solid/liquid interfaces. The minimum detectable mass change is typically ~1 ng·cm^{-2}. Besides, QCM-D complements conventional QCM by simultaneously measuring changes in frequency, f, and dissipation factor, D. QCM-D uses a disk-shaped, AT-cut piezoelectric quartz as a sensor, which is usually coated with thin gold films on both sides.[127]

During a QCM-D experiment, an external driving oscillating circuit is applied to the quartz crystal through its gold electrodes and excites the crystal. The crystal starts to oscillate in shear mode at its fundamental resonant frequency, as shown in Figure 2.13.[120] The driver circuit

is periodically disconnected *via* a computer-controlled relay, inducing an exponential damped sinusoidal decay in the oscillating amplitude

$$A(t) = A_0 e^{-t/\tau} \sin(2\pi ft + \varphi) \qquad [2.13]$$

where A_0 is the amplitude at $t = 0$, τ is the decay time constant, f is the oscillation frequency and φ is the phase. The dissipation factor, D, is inversely proportional to τ:

$$D = \frac{1}{\pi f \tau} \qquad [2.14]$$

D is also defined as

$$D = \frac{E_{dissipated}}{2\pi E_{stored}} \qquad [2.15]$$

where $E_{dissipated}$ is the energy dissipated during one period of oscillation, and E_{stored} is the energy stored in the system. If the adsorbed film is viscous, energy will dissipate because of friction between the adsorbed film and the electrodes of the quartz crystal. Thus, D contains information about the viscoelastic properties of the adsorbed film. By recording the decay curve, the dissipation factor D, the free oscillation frequency of the crystal, and the oscillation amplitude are obtained.[128-129]

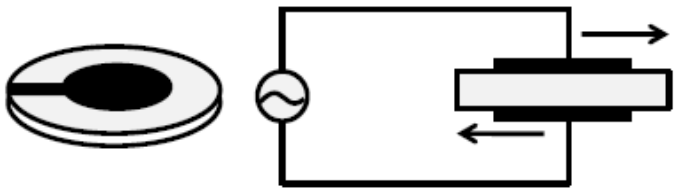

Figure 2.13. Gold-coated QCM quartz crystal oscillating in shear mode. (Reprinted from ref 120; fair use; Copyright 2010 Liu Z)

2.7.2.1. Sauerbrey model

The frequently applied Sauerbrey model postulates that an adsorbed film on the electrode of a piezoelectric quartz crystal will induce a decrease in the oscillation frequency of the crystal. The change in oscillating frequency is linearly proportional to the applied mass:[130]

$$\Delta m = -\frac{\rho_q t_q \Delta f}{f_0 n} = -\frac{\rho_q v_q \Delta f}{2 f_0^{\,2} n} = -\frac{C}{n}\Delta f \qquad [2.16]$$

where ρ_q is the density of quartz, t_q is the thickness of the quartz disc, f_0 is the fundamental resonant frequency of the first overtone (n = 1), n is the overtone number (n = 1, 3, 5, 7…), and v_q is the shear wave velocity in quartz. With ρ_q = 2648 kg·m^{-3}, v_q = 3340 m·s^{-1}, and f_0 = 5 MHz, the mass sensitivity constant, C, becomes 17.7 ng·cm^{-2}·Hz^{-1}.The Sauerbrey model holds when (i) the applied mass is relatively small compared to the mass of the crystal, (ii) the adsorbed mass is evenly distributed over the electrode of the crystal, and (iii) the adsorbed film does not slide on the QCM-D electrode.[129] Hence, the Sauerbrey model is valid when the adsorbed film is rigid ($\Delta D < 1\cdot10^{-6}$ per 10 Hz frequency change) and can be treated as part of the crystal itself. However, for non-rigid adsorbed films, the Sauerbrey model is no longer valid because the frequency change not only depends on the applied mass, but also on energy dissipation. In order to accurately analyze the QCM-D data for viscoelastic adsorbed layer, a viscoelastic model needs to be applied.

2.7.3. Atomic force microscopy

Atomic force microscopy (AFM) is a powerful topographic characterization tool for imaging and measuring surfaces at micro- or nano-level resolution. Its provides high-resolution

images for different material surfaces, such as metals, ceramics, polymers, biomolecules, and cells.[131-135]

The key component of AFM instruments is a micro-machined cantilever with an ultra-sharp, low spring constant tip at one end, which interacts with the sample surface. Most common tips are made of silicon or silicon nitride. Silicon nitride tips have radii in the range from 10 to 20 nm, and the radii of silicon tips are around 10 nm.[136] The cantilever is always mounted to piezoelectric actuators. Piezoelectric actuators change shape in response to an applied electric field and are thus able to convert electrical voltage to mechanical motion in a desired direction.

Figure 2.14. shows the configuration of an Asylum Research MFP-3D atomic force microscope. In this configuration, the sample in mounted on independent X, Y piezoelectric scanners and moves in the X-Y plane, while the cantilever is connected to a piezoelectric scanner that moves in the z-direction.

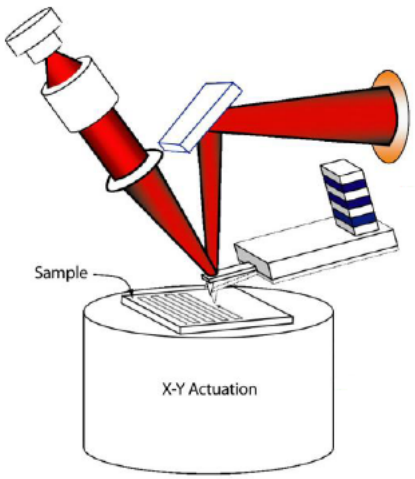

Figure 2.14. Configuration of the Asylum Research MFP-3D atomic force microscope. (Reprinted from ref [137]; fair use; Copyright 2008 Asylum Research)

During an AFM experiment, the cantilever tip approaches the sample surface gradually until the distance decreases to a couple of Ångströms. When the distance is large, the tip experiences a weakly attractive force. As the distance decreases, the repulsive force starts to dominate, as shown in the Figure 2.15. The tip bends under the interaction force, and the deflection of the tip is monitored with a laser beam impinging on the back of the cantilever and being reflected into a position sensitive photo detector. This method is used to maintain the tip interacting with the sample surface with a constant force or at a constant height.[138]

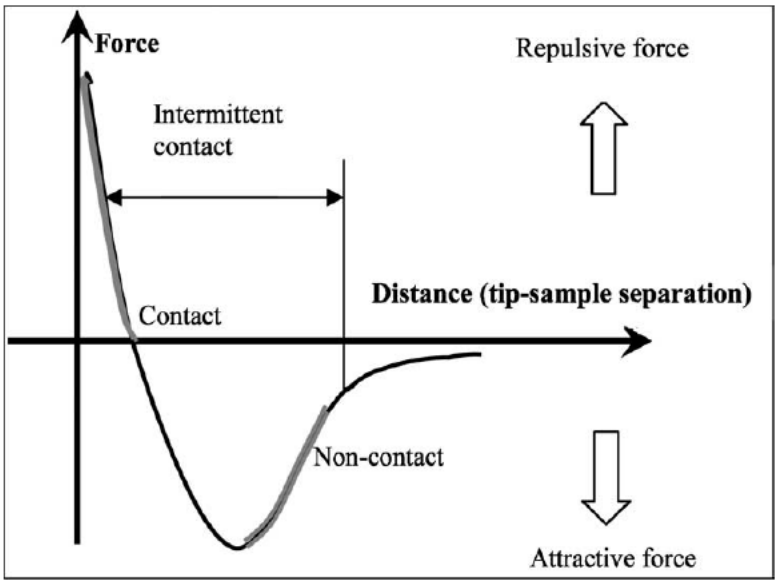

Figure 2.15. Interaction force variation versus distance between AFM tip and sample. (Reprinted from ref 138; fair use; Copyright 2004 Elsevier)

AFMs can operate in three modes to obtain an image of the surface landscape: contact mode, non-contact mode, and tapping mode. Figure 2.16 depicts the operation in all three modes and the surface topography generated in each mode.[138]

i) ii) iii)

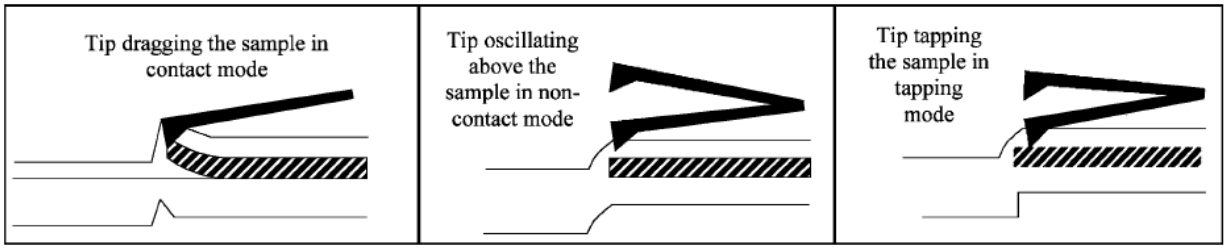

Figure 2.16. AFM operation modes: (i) contact mode, (ii) non-contact mode and (iii) tapping mode. (Reprinted from ref 138; fair use; Copyright 2004 Elsevier)

Contact mode operates in the region of strong repulsive forces between the tip and the surface. In this mode, the tip is in soft "physical contact" with the sample surface as it scans the surface. There are two ways to obtain the topography in this mode: constant force mode and variable force mode. In constant force mode, the feedback loop compares the deflection signal with the set point and adjust the voltage applied to the Z-piezoelectric scanner to maintain the cantilever deflection. The topography is derived from the voltage applied to the scanner. In variable force mode, the feedback loop is disabled and the cantilever deflects freely during the scan. The topography height image is the deflection signal of the cantilever.[136] Because the lateral friction force applied by the tip can be on the order of nN, which is large enough to damage soft surfaces like biomaterials and polymers, contact mode is not suitable for imaging of soft surfaces.[133]

In non-contact mode, the cantilever is away from sample surface and a weakly attractive force is in effect. The cantilever oscillates close to its resonant frequency with a certain amplitude. During scanning, while the drive frequency is maintained constant, both the oscillation frequency and amplitude of the tip will change because of its interactions with the sample surface. The amplitude of oscillation (set point) is maintained by changing the voltage

applied to the z-piezoelectric scanner, keeping a constant tip-surface distance. Since a low lateral force is applied to the sample surface, non-contact mode will cause no damage to sample surfaces and is more suitable for measuring soft and elastic samples, compared to contact model.[136]

In tapping mode, the tip–sample interaction is in the contact and non-contact region intermittently.[136] The cantilever oscillates at an amplitude of 20–100 nm when the tip is not in contact with the sample surface. During scanning, it moves towards the surface and starts to tap the surface at a frequency of 50–500 kHz. This interaction leads to a reduction in the oscillation amplitude, which is used to obtain the topographic features.[133] Tapping mode allows high-resolution imaging of soft samples, although its scan speed is lower than contact mode.[138]

2.8. References

(1) Reiter, W.-D. *Curr. Opin. Plant Biol.* **2002**, *5*, 536.

(2) Cosgrove, D. J. *Nat. Rev. Mol. Cell Biol.* **2005**, *6*, 850.

(3) Yarbrough, J. M.; Himmel, M. E.; Ding, S.-Y. *Biotechnol. Biofuels* **2009**, *2*, 17.

(4) McNeil, M.; Darvill, A. G.; Fry, S. C.; Albersheim, P. *Annu. Rev. Biochem.* **1984**, *53*, 625.

(5) Whitney, S. E. C.; Gothard, M. G. E.; Mitchell, J. T.; Gidley, M. J. *Plant Physiol.* **1999**, *121*, 657.

(6) Perez, J.; Munoz-Dorado, J.; de, l. R. T.; Martinez, J. *Int. Microbiol.* **2002**, *5*, 53.

(7) Saka, S. K. *Wood and Cellulosic Chemistry*; 2nd ed. ed.; Marcel Dekker, Inc: New York, N.Y., 2001.

(8) Hon, D. N. S.; Shiraishi, N.; Editors *Wood and Cellulosic Chemistry*; Marcel Dekker, Inc., 1991.

(9) Keegstra, K.; Talmadge, K. W.; Bauer, W. D.; Albersheim, P. *Plant Physiol.* **1973**, *51*, 188.

(10) Fry, S. C. *Physiol. Plant.* **1989**, *75*, 532.

(11) Hayashi, T. *Annu. Rev. Plant Physiol. Plant Mol. Biol.* **1989**, *40*, 139.

(12) Hayashi, T.; Marsden, M. P. F.; Delmer, D. P. *Plant Physiol.* **1987**, *83*, 384.

(13) Talbott, L. D. R., Peter M. *Plant Physiol.* **1992**, *98*, 357.

(14) Ha, M.-A.; Apperley, D. C.; Jarvis, M. C. *Plant Physiol.* **1997**, *115*, 593.

(15) Cosgrove, D. J. *Plant Physiol.* **2001**, *125*, 131.

(16) Dick-Perez, M.; Zhang, Y.; Hayes, J.; Salazar, A.; Zabotina, O. A.; Hong, M. *Biochemistry* **2011**, *50*, 989.

(17) Hayashi, T. *Annu. Rev. Plant Physiol. Plant Mol. Biol.* **1989**, *40*, 139.

(18) Staudinger, H. *Ber. Dtsch. Chem. Ges. B* **1920**, *53B*, 1073.

(19) Klemm, D.; Heublein, B.; Fink, H.-P.; Bohn, A. *Angew. Chem., Int. Ed.* **2005**, *44*, 3358.

(20) Jeronimidis, G. *Symp Soc Exp Biol* **1980**, *34*, 169.

(21) O'Sullivan, A. C. *Cellulose (London)* **1997**, *4*, 173.

(22) Kontturi, E.; Tammelin, T.; Osterberg, M. *Chem. Soc. Rev.* **2006**, *35*, 1287.

(23) Jarvis, M. *Nature (London, U. K.)* **2003**, *426*, 611.

(24) Atalla, R. H.; VanderHart, D. L. *Science (Washington, D. C., 1883-)* **1984**, *223*, 283.

(25) Nishiyama, Y.; Sugiyama, J.; Chanzy, H.; Langan, P. *J. Am. Chem. Soc.* **2003**, *125*, 14300.

(26) Peng, B. L.; Dhar, N.; Liu, H. L.; Tam, K. C. *Can. J. Chem. Eng.* **2011**, *89*, 1191.

(27) Araki, J.; Wada, M.; Kuga, S.; Okano, T. *Colloids Surf., A* **1998**, *142*, 75.

(28) Habibi, Y.; Lucia, L. A.; Rojas, O. J. *Chem. Rev. (Washington, DC, U. S.)* **2010**, *110*, 3479.

(29) Araki, J.; Wada, M.; Kuga, S. *Langmuir* **2001**, *17*, 21.

(30) Beck-Candanedo, S.; Roman, M.; Gray, D. G. *Biomacromolecules* **2005**, *6*, 1048.

(31) de, M. A. J.; Siqueira, G.; Curvelo, A. A. S.; Dufresne, A. *Polymer* **2009**, *50*, 4552.

(32) De, S. L. M. M.; Borsali, R. *Macromol. Rapid Commun.* **2004**, *25*, 771.

(33) Garcia, d. R. N. L.; Thielemans, W.; Dufresne, A. *Cellulose (Dordrecht, Neth.)* **2006**, *13*, 261.

(34) Kimura, F.; Kimura, T.; Tamura, M.; Hirai, A.; Ikuno, M.; Horii, F. *Langmuir* **2005**, *21*, 2034.

(35) Miller, A. F.; Donald, A. M. *Biomacromolecules* **2003**, *4*, 510.

(36) Pranger, L.; Tannenbaum, R. *Macromolecules (Washington, DC, U. S.)* **2008**, *41*, 8682.

(37) Revol, J. F. *Carbohydr. Polym.* **1982**, *2*, 123.

(38) Revol, J. F.; Bradford, H.; Giasson, J.; Marchessault, R. H.; Gray, D. G. *Int. J. Biol. Macromol.* **1992**, *14*, 170.

(39) Azizi Samir, M. A. S.; Alloin, F.; Dufresne, A. *Biomacromolecules* **2005**, *6*, 612.

(40) Sugiyama, J.; Chanzy, H.; Maret, G. *Macromolecules* **1992**, *25*, 4232.

(41) Favier, V.; Canova, G. R.; Cavaille, J. Y.; Chanzy, H.; Dufreshne, A.; Gauthier, C. *Polym. Adv. Technol.* **1995**, *6*, 351.

(42) Habibi, Y.; Dufresne, A. *Biomacromolecules* **2008**, *9*, 1974.

(43) Habibi, Y.; Goffin, A.-L.; Schiltz, N.; Duquesne, E.; Dubois, P.; Dufresne, A. *J. Mater. Chem.* **2008**, *18*, 5002.

(44) Azizi, S. M. A. S.; Chazeau, L.; Alloin, F.; Cavaille, J. Y.; Dufresne, A.; Sanchez, J. Y. *Electrochim. Acta* **2005**, *50*, 3897.

(45) Samir, M. A. S. A.; Alloin, F.; Sanchez, J.-Y.; Dufresne, A. *Polim.: Cienc. Tecnol.* **2005**, *15*, 109.

(46) Azizi, S. M. A. S.; Alloin, F.; Sanchez, J.-Y.; Dufresne, A. *Polymer* **2004**, *45*, 4149.

(47) Grunert, M.; Winter, W. T. *J. Polym. Environ.* **2002**, *10*, 27.

(48) Petersson, L.; Mathew, A. P.; Oksman, K. *J. Appl. Polym. Sci.* **2009**, *112*, 2001.

(49) Choi, Y.; Simonsen, J. *J. Nanosci. Nanotechnol.* **2006**, *6*, 633.

(50) Chazeau, L.; Cavaille, J. Y.; Canova, G.; Dendievel, R.; Boutherin, B. *J. Appl. Polym. Sci.* **1999**, *71*, 1797.

(51) Chazeau, L.; Cavaille, J. Y.; Terech, P. *Polymer* **1999**, *40*, 5333.

(52) Chazeau, L.; Paillet, M.; Cavaille, J. Y. *J. Polym. Sci., Part B: Polym. Phys.* **1999**, *37*, 2151.

(53) Klemm, D.; Kramer, F.; Moritz, S.; Lindström, T.; Ankerfors, M.; Gray, D.; Dorris, A. *Angewandte Chemie International Edition* **2011**, *50*, 5438.

(54) Roman, M.; Dong, S.; Hirani, A.; Lee, Y. W. *ACS Symp. Ser.* **2009**, *1017*, 81.

(55) Kovacs, T.; Naish, V.; O'Connor, B.; Blaise, C.; Gagne, F.; Hall, L.; Trudeau, V.; Martel, P. *Nanotoxicology* **2010**, *4*, 255.

(56) Dong, S.; Roman, M. *J. Am. Chem. Soc.* **2007**, *129*, 13810.

(57) Roman, M. In *Model Cellulosic Surfaces*; American Chemical Society: 2009; Vol. 1019, p 3.

(58) Roberts, G.; Editor *Langmuir-Blodgett Films*; Plenum, 1990.

(59) Kistler, S. F.; Schweizer, P. M.; Editors *Liquid Film Coating: Scientific Principles and their Technological Implications*; Chapman & Hall, 1997.

(60) Schaub, M.; Wenz, G.; Wegner, G.; Stein, A.; Klemm, D. *Adv. Mater. (Weinheim, Fed. Repub. Ger.)* **1993**, *5*, 919.

(61) Gunnars, S.; Wagberg, L.; Cohen, S. M. A. *Cellulose (Dordrecht, Neth.)* **2002**, *9*, 239.

(62) Faelt, S.; Wagberg, L.; Vesterlind, E. L.; Larsson, P. T. *Cellulose (Dordrecht, Neth.)* **2004**, *11*, 151.

(63) Kontturi, E.; Thune, P. C.; Niemantsverdriet, J. W. *Polymer* **2003**, *44*, 3621.

(64) Edgar, C. D.; Gray, D. G. *Cellulose (Dordrecht, Neth.)* **2003**, *10*, 299.

(65) Lefebvre, J.; Gray, D. G. *Cellulose (Dordrecht, Neth.)* **2005**, *12*, 127.

(66) Kontturi, E.; Thuene, P. C.; Niemantsverdriet, J. W. *Langmuir* **2003**, *19*, 5735.

(67) Scheller, H. V.; Ulvskov, P. *Annu. Rev. Plant Biol.* **2010**, *61*, 263.

(68) Ebringerova, A.; Hromadkova, Z.; Heinze, T. *Adv. Polym. Sci.* **2005**, *186*, 1.

(69) Sun, R. S., X. F.; Tomkinson, J.; Gatenholm, P., Tenkanen, M., Ed.; American Chemical Society: Washington, D. C.: Washington, D. C., 2004; Vol. 864, p 3.

(70) Collins, P. F., R.; John Wiley& Sons.: New York, 1995, p 463.

(71) Popa, V. I.; Dumitriu, S., Ed.; Marcel Dekker, Inc.: New York, 1996, p 107.

(72) Singh, S. K. G., R. A. In *Biopolymers from Polysaccharides and Agroproteins.*

; Gross, R. A., Scholz, C., Ed.; American Chemical Society: Washington, D. C.: Washington, D. C., 2001; Vol. 786, p 9.

(73) Warren, R. A. J. *Annu. Rev. Microbiol.* **1996**, *50*, 183.

(74) Kleman-Leyer, K. M.; Siika-Aho, M.; Teeri, T. T.; Kirk, T. K. *Appl. Environ. Microbiol.* **1996**, *62*, 2883.

(75) Kleman-Leyer, K. M.; Gilkes, N. R.; Miller, R. C., Jr.; Kirk, T. K. *Biochem. J.* **1994**, *302*, 463.

(76) Staehlberg, J.; Divne, C.; Koivula, A.; Piens, K.; Claeyssens, M.; Teeri, T. T.; Jones, T. A. *J. Mol. Biol.* **1996**, *264*, 337.

(77) Divne, C.; Staahlberg, J.; Reinikainen, T.; Ruohonen, L.; Pettersson, G.; Knowles, J. K. C.; Teeri, T. T.; Jones, T. A. *Science (Washington, D. C.)* **1994**, *265*, 524.

(78) Rouvinen, J.; Bergfors, T.; Teeri, T.; Knowles, J. K. C.; Jones, T. A. *Science (Washington, D. C., 1883-)* **1990**, *249*, 380.

(79) Terri, T. T. *Trends Biotechnol.* **1997**, *15*, 160.

(80) Lynd, L. R.; Weimer, P. J.; van, Z. W. H.; Pretorius, I. S. *Microbiol. Mol. Biol. Rev.* **2002**, *66*, 506.

(81) Staahlberg, J.; Johansson, G.; Pettersson, G. *Bio/Technology* **1991**, *9*, 286.

(82) Teeri, T. T.; Koivula, A.; Linder, M.; Wohlfahrt, G.; Divne, C.; Jones, T. A. *Biochem. Soc. Trans.* **1998**, *26*, 173.

(83) Gilbert, H. J.; Hazlewood, G. P. *J. Gen. Microbiol.* **1993**, *139*, 187.

(84) Tomme, P.; Warren, R. A.; Gilkes, N. R. *Adv Microb Physiol* **1995**, *37*, 1.

(85) Mandels, M. R., E. T. *J. Bacteriol.* **1957**, *73*, 269.

(86) Nogawa, M.; Goto, M.; Okada, H.; Morikawa, Y. *Curr. Genet.* **2001**, *38*, 329.

(87) Takashima, S.; Nakamura, A.; Hidaka, M.; Masaki, H.; Uozumi, T. *Journal of Biochemistry* **1999**, *125*, 728.

(88) Chanzy, H.; Henrissat, B. *FEBS Lett.* **1985**, *184*, 285.

(89) Palonen, H.; Tenkanen, M.; Linder, M. *Appl. Environ. Microbiol.* **1999**, *65*, 5229.

(90) Jeoh, T.; Wilson, D. B.; Walker, L. P. *Biotechnol. Prog.* **2002**, *18*, 760.

(91) Carrard, G.; Linder, M. *Eur. J. Biochem.* **1999**, *262*, 637.

(92) Linder, M.; Teeri, T. T. *Proc. Natl. Acad. Sci. U. S. A.* **1996**, *93*, 12251.

(93) Medve, J.; Stahlberg, J.; Tjerneld, F. *Appl. Biochem. Biotechnol.* **1997**, *66*, 39.

(94) Fainerman, V. B.; Moebius, D.; Miller, R.; Editors *Surfactants: Chemistry, Interfacial Properties, Applications. [In: Stud. Interface Sci., 2001; 13]*; Elsevier Science B.V., 2001.

(95) Levitz, P. E. *Colloids Surf., A* **2002**, *205*, 31.

(96) Rosen, M. J. *Surfactants and Interfacial Phenomena, 3rd Edition*; John Wiley & Sons, 2004.

(97) Partyka, S.; Zaini, S.; Lindheimer, M.; Brun, B. *Colloids Surf.* **1984**, *12*, 255.

(98) Levitz, P.; El, M. A.; Keravis, D.; Van, D. H. *J. Colloid Interface Sci.* **1984**, *99*, 484.

(99) Lindheimer, M.; Keh, E.; Zaini, S.; Partyka, S. *J. Colloid Interface Sci.* **1990**, *138*, 83.

(100) Levitz, P.; Van Damme, H. *The Journal of Physical Chemistry* **1986**, *90*, 1302.

(101) Levitz, P.; Van Damme, H.; Keravis, D. *The Journal of Physical Chemistry* **1984**, *88*, 2228.

(102) Lee, E. M.; Thomas, R. K.; Cummins, P. G.; Staples, E. J.; Penfold, J.; Rennie, A. R. *Chem. Phys. Lett.* **1989**, *162*, 196.

(103) Dong, J.; Mao, G. *Langmuir* **2000**, *16*, 6641.

(104) Rutland, M. W.; Senden, T. J. *Langmuir* **1993**, *9*, 412.

(105) Grant, L. M.; Ducker, W. A. *The Journal of Physical Chemistry B* **1997**, *101*, 5337.

(106) Patrick, H. N.; Warr, G. G.; Manne, S.; Aksay, I. A. *Langmuir* **1997**, *13*, 4349.

(107) Levitz, P. *Langmuir* **1991**, *7*, 1595.

(108) Bohmer, M. R.; Koopal, L. K. *Langmuir* **1990**, *6*, 1478.

(109) Love, J. C.; Estroff, L. A.; Kriebel, J. K.; Nuzzo, R. G.; Whitesides, G. M. *Chem. Rev. (Washington, DC, U. S.)* **2005**, *105*, 1103.

(110) Ulman, A. *Chem. Rev. (Washington, D. C.)* **1996**, *96*, 1533.

(111) Bain, C. D.; Evall, J.; Whitesides, G. M. *J. Am. Chem. Soc.* **1989**, *111*, 7155.

(112) Bain, C. D.; Whitesides, G. M. *Science (Washington, D. C., 1883-)* **1988**, *240*, 62.

(113) Dubois, L. H.; Nuzzo, R. G. *Annu. Rev. Phys. Chem.* **1992**, *43*, 437.

(114) Nuzzo, R. G.; Allara, D. L. *J. Am. Chem. Soc.* **1983**, *105*, 4481.

(115) Poirier, G. E.; Pylant, E. D. *Science (Washington, D. C.)* **1996**, *272*, 1145.

(116) Porter, M. D.; Bright, T. B.; Allara, D. L.; Chidsey, C. E. D. *J. Am. Chem. Soc.* **1987**, *109*, 3559.

(117) Bain, C. D.; Troughton, E. B.; Tao, Y. T.; Evall, J.; Whitesides, G. M.; Nuzzo, R. G. *J. Am. Chem. Soc.* **1989**, *111*, 321.

(118) Schasfoort, R. B. M.; McWhirter, A.; Royal Society of Chemistry: 2008, p 35.

(119) Cooper, M. A. *Nat. Rev. Drug Discovery* **2002**, *1*, 515.

(120) Liu, Z., Virginia Polytechnic Institute and State University, 2010.

(121) Salamon, Z.; Macleod, H. A.; Tollin, G. *Biochim. Biophys. Acta, Rev. Biomembr.* **1997**, *1331*, 131.

(122) Green, R. J.; Frazier, R. A.; Shakesheff, K. M.; Davies, M. C.; Roberts, C. J.; Tendler, S. J. *Biomaterials* **2000**, *21*, 1823.

(123) Sambles, J. R.; Bradbery, G. W.; Yang, F. *Contemp. Phys.* **1991**, *32*, 173.

(124) van, K. D. W.; Editor *Properties of Polymers: Their Correlation with Chemical Structure; Their Numerical Estimation and Prediction from Additive Group Contributions, Third Completely Revised Edition*; Elsevier, 1997.

(125) De, F. J. A.; Benjamins, J.; Veer, F. A. *Biopolymers* **1978**, *17*, 1759.

(126) Sigal, G. B.; Mrksich, M.; Whitesides, G. M. *Langmuir* **1997**, *13*, 2749.

(127) Hoeoek, F.; Rodahl, M.; Brzezinski, P.; Kasemo, B. *Langmuir* **1998**, *14*, 729.

(128) Rodahl, M.; Hook, F.; Krozer, A.; Brzezinski, P.; Kasemo, B. *Rev. Sci. Instrum.* **1995**, *66*, 3924.

(129) Rodahl, M.; Kasemo, B. *Sensors and Actuators A: Physical* **1996**, *54*, 448.

(130) Sauerbrey, G. *Z. Phys.* **1959**, *155*, 206.

(131) DeRose, J. A.; Revel, J. P. *Thin Solid Films* **1998**, *331*, 194.

(132) Orisaka, S.; Minobe, T.; Uchihashi, T.; Sugawara, Y.; Morita, S. *Appl. Surf. Sci.* **1999**, *140*, 243.

(133) Jandt, K. D. *Surf. Sci.* **2001**, *491*, 303.

(134) Baretzky, B.; Reinsch, B.; Taeffner, U.; Schneider, G.; Ruehle, M. *Z. Metallkd.* **1996**, *87*, 332.

(135) Klinov, D. V.; Lagutina, I. V.; Prokhorov, V. V.; Neretina, T.; Khil, P. P.; Lebedev, Y. B.; Cherny, D. I.; Demin, V. V.; Sverdlov, E. D. *Nucleic Acids Res.* **1998**, *26*, 4603.

(136) Zavala, G. *Colloid Polym. Sci.* **2008**, *286*, 85.

(137) *MFP-3D Manual*; In Version 04-08 ed.; Asylum Research, 2008.

(138) Jalili, N.; Laxminarayana, K. *Mechatronics* **2004**, *14*, 907.

CHAPTER 3

Cellulose morphology and surface charge effects on xyloglucan adsorption

3.1. Abstract

Elucidating the interactions between cellulose and hemicelluloses is of fundamental importance for understanding the molecular architecture of plant cell walls. In this study, the amount of xyloglucan (XG) adsorbed onto uncharged desulfated nanocrystalline cellulose (DNC) thin films was quantified by quartz crystal microbalance with dissipation monitoring (QCM-D) and surface plasmon resonance (SPR). The morphology of the cellulose substrates before and after XG adsorption was imaged via atomic force microscope (AFM). XG adsorption showed strong dependence on DNC film thickness, and XG adsorption isotherms were effectively fitted by the Freundlich model. A comparison of the results with those of my colleagues Joshua D. Kittle and Emma Edgar[1] for negatively charged sulfated nanocrystalline cellulose (SNC) films and amorphous regenerated cellulose (RC) films allows the conclusion that cellulose morphology and surface charge of the substrate play a limited role in XG adsorption and that accessible surface area of the cellulose film may be the factor leading to apparent differences in XG adsorption for different surfaces.

3.2. Introduction

Biomass provides materials for textiles, paper, adhesives, films, thickeners and other products.[2-3] Recently it has attracted great interest as a potential source for sustainable biofuel

due to the high worldwide demand for energy, unreliable petroleum sources, and concern over global climate change.[4] The primary plant cell walls are natural composites. Understanding the interactions between primary plant cell wall components, such as cellulose and XG, could facilitate the extraction and use of these renewable materials.[5]

The constituent polymers of the primary plant cell wall can be classified as cellulose, hemicelluloses, and pectins. The unbranched cellulose chains pack together by hydrogen bonding to form cellulose microfibrils with a diameter of ~ 4 nm. Within primary plant cell walls, the cellulose microfibril layers arrange 10–20 nm apart from each other, and hemicelluloses connect the microfibril layers via non-covalent bonding. The pectic polysaccharides form a separate network in the presence of calcium ions. The pectin network is generally less rigid than the hemicellulose network.[6-7]

XG, the dominant hemicellulose in primary plant cell walls, is believed to attach to cellulose microfibrils via hydrogen bonding[7] and perform a critical role in load-bearing network formation.[8] However, the binding capacity of XG to cellulose in native primary plant cell walls remains unclear. Due to the complexity of plant cell walls and the difficulty of studying XG–cellulose interactions *in situ,* research efforts have focused on investigating the adsorption of extracted XG on cellulose from various sources.[9-13] Brumer *et al*. studied the adsorption of XG on cotton cellulose using a colorimetric method and reported a value of 11 mg XG·g^{-1} cellulose.[9] Lopez *et al*. used the same method to measure the adsorption of XG on bacterial microcrystalline cellulose (BMCC) but reported a value of 0.27 mg XG·g^{-1} cellulose.[11] The large discrepancy between the reported adsorption amounts is possibly due to the difference in the surface area of cellulose substrates, as indicated by Brumer and Hayashi.[9,14] Adsorbed XG in units of mg

$XG \cdot m^{-2}$ cellulose have also been reported. For instance, Cerclier *et al.* studied the adsorption of XG onto sulfated cellulose nanocrystal thin films using QCM-D and found that the amount of adsorbed XG equaled 26 mg $XG \cdot m^{-2}$ cellulose. Nevertheless, it is still ambiguous whether the surface charge of cellulose influences XG adsorption.[10-11] Consequently, cellulose model substrates with controlled cellulose morphology and surface charge need to be prepared to quantify the binding capacity of XG to cellulose.

In this study, three cellulose model thin films were used: non-charged desulfated nanocrystalline cellulose (DNC) was prepared by me, negatively charged sulfated nanocrystalline cellulose (SNC), and amorphous, regenerated cellulose (RC) thin films were prepared by Joshua D. Kittle and Emma Edgar.[1] QCM-D and SPR were used to study the dependence of XG adsorption onto cellulose films of variable thickness and obtain XG adsorption isotherms. Results obtained from the three cellulose films were compared to investigate the effects of cellulose morphology and charge on XG adsorption.

3.3. Experimental section

3.3.1. Materials

Dissolving-grade softwood sulfite pulp (Temalfa 93A-A) was kindly provided by Tembec, Inc. 11-amino-1-undecanethiol hydrochloride (99+%, 1 mmol/L) was purchased from Asemblon. Sulfuric acid (95.9 wt %, Certified ACS Plus), sodium hydroxide (0.1 N, Certified), sodium chloride (Certified ACS), hydrogen peroxide (34–37%, Technical grade), ammonium hydroxide (28.9%, Certified ACS Plus), pyridine (99.5%, Chemservice), DMSO (Certified ACS), methanol (99.8%, Acros Organics), and ethanol (200 proof) were purchased from Fisher Scientific. XG from tamarind seeds was purchased from Megazyme, Inc. (202 kDa, lot 00401b).

All water used was deionized (DI) water with a resistivity of 18.2 MΩ·cm, obtained from a Millipore Direct-Q 5 Ultrapure Water Systems.

3.3.2. Preparation of sulfated nanocrystalline cellulose (SNC)

H_2SO_4-hydrolyzed SNC suspension was prepared following the method of Revol *et al.* with minor modifications.[15] Lapsheets of the sulfite pulp were cut into small pieces, milled in a Thomas Wiley Mini-Mill (Thomas Scientific), and passed through a 60-mesh screen for the removal of large particles. Five hundred milliliters of 64 wt% H_2SO_4 was preheated to 45 °C and added to 50 g of milled pulp in a 1 L round-bottom flask. The acid hydrolysis reaction was carried out at 45 °C for 60 min under mechanical stirring and was quenched by dilution of the acid–pulp mixture with 3 L cold DI water. The acid–pulp mixture was centrifuged at 25 °C and 4900 rpm for 15 min with a Thermo IEC Centra-GP8R refrigerated centrifuge (Thermo Fisher Scientific, Inc.). After centrifugation, the acid-containing supernatant was removed and the sediment was collected. The sediment was then transferred to Spectra/Por 4 dialysis tubing (Spectrum Lab, Inc) and dialyzed against DI water until a constant dialysate pH value was reached. After dialysis, the SNC suspension was sonicated for 5 min at 40% amplitude with a 500 W ultrasonic processor (VC 505, Sonics & Materials, Inc) and filtered through 1.0 μm and 0.45 μm poly(vinylidene fluoride) syringe filters (Whatman, Ltd).

3.3.3. Preparation of desulfated nanocrystalline cellulose (DNC) via solvolytic desulfation

The solvolytic desulfation reaction of SNC was carried out following the method of Jiang *et al.*[16] Pyridine was added drop by drop to a 0.78 wt% SNC suspension until its pH reached 5.5–6. In this step, the sulfate groups on the SNC surface were converted into pyridinium salts. The

resulting suspension was lyophilized with a Freezone 4.5L freeze-dry system (Labconco Corp). Two grams of the freeze-dried SNC sample was dispersed in 180 mL DMSO overnight, and the obtained homogeneous suspension was sonicated for 5 min at 40% amplitude. After addition of 20 mL of methanol, the temperature of the reaction mixture was raised to 80 °C with a water bath, and the desulfation reaction was carried out for 2 h under mechanical stirring. The reaction was quenched by immersion of the reaction flask into an ice bath and dilution of the reaction mixture with 200 mL room temperature DI water. The resulting DNC suspension was transferred to dialysis tubing and dialyzed against DI water for two weeks, until all unreacted pyridine molecules had been removed. The resulting DNC suspension was filtered through a 0.45 μm syringe filter and finally concentrated to 1 wt% by rotavapor (R-200/205, BUCHI inc).

3.3.4. Conductometric titration

SNC and DNC suspensions of 0.78 and 1 wt%, respectively, were used for conductometric titration. For the titration, 50 mL cellulose nanocrystal suspension was placed in a 100 mL three-neck round bottom flask. A S47 SevenMulti pH/conductivity meter (Mettler-Toledo) connected to a pH electrode (Inlab 413, Mettler-Toledo International, Inc.) and a conductivity electrode (Inlab 730, Mettler-Toledo International, Inc.) was used to monitor the pH and conductivity values. 0.02 N NaOH was used as the titrant and titrations were carried out in triplicate under nitrogen.

The surface charge density, σ, in the unit of mequiv·g^{-1} was calculated from the volume of NaOH added as

$$\sigma = \frac{c_{NaOH} \cdot V_{NaOH}}{c_{CNC} \cdot \alpha_{CNC}} \qquad [3.1]$$

where c_{NaOH} is the concentration of the titrant, V_{NaOH} is the volume of titrant used when reaching the equivalence point, c_{CNC} is the concentration of the cellulose nanocrystal suspension (SNC or DNC), and α_{CNC} is the mass of CNC suspension titrated.

3.3.5. Preparation and characterization of DNC thin films

3.3.5.1. Substrate cleaning

Gold QCM-D (Q-sense AB, gold, 5 MHz) and SPR (Reichert, gold) sensor chips were cleaned by exposure of the gold surface to UV/ozone for 20 min. After rising of the surface with DI water, the sensor chips were immersed into a 1:1:5 v/v solution of NH_4OH:H_2O_2:DI water at 80 °C for 1 h. Following another 20 min UV/ozone treatment, the sensor chips were rinsed with DI water and dried with N_2.

3.3.5.2. DNC film deposition

The gold surface was treated with 1 mM 11-amino-1-undecanol ethanol solution for at least 24 h. The resulting amine-terminated alkanethiol self-assembled monolayer (SAM-NH_2) helped anchor the cellulose nanocrystals to the gold surface. DNC films with different thicknesses were spin-coated (WS-400A-6NPP-Lite, Laurell Technologies Corp.) from DNC suspensions with concentrations from 0.5 wt% to 1.0 wt% for 60 s at different spinning speeds (4000 rpm to 6000 rpm). The so formed films were stabilized by heat treatment in a vacuum oven at 65 °C overnight and characterized in terms of film thickness and morphology by ellipsometry and AFM, respectively.

3.3.5.3. Ellipsometry measurements

DNC film thickness was determined with a multi-angle of incidence ellipsometer (Picometer Ellipsometer, Beaglehole Instruments) equipped with a single wavelength (633 nm) laser light source. The angle of incidence was varied between 60 and 80° with 1° steps. The film

thickness was modeled with TFCompanion software (Semiconsoft) assuming a refractive index of 1.51 for the DNC film. The reported thickness values are means ± one standard deviation from measurements at three different locations on the film.

3.3.5.4. Atomic force microscopy (AFM)

An Asylum Research AFM (MFP-3D-BIO, Asylum Research) was used for AFM imaging. During AFM measurements, height images were obtained under ambient conditions (22 °C, 50% humidity) with OMCL-AC160TS standard silicon probes (Olympus Corp.). The roughness of the height images was calculated by the MFP-3D software as the root mean square value of all collected height values in the scanned area.

3.3.6. Surface plasmon resonance (SPR)

An SR7000 (Reichert Inc.) SPR system was employed to detect the "dry mass" (or "optical mass") of XG adsorbed onto the DNC films. The thickness of each film was first determined by ellipsometry before the sensor slide was placed into the SPR flow cell. Both water and XG solution were degassed before they were introduced into the flow cell. The flow rate was set at 0.200 mL·min^{-1} and the temperature of the solutions was 25 °C. A switch valve was used to switch between water and XG solution. Care was taken when switching solutions to avoid introducing air bubbles into the flow cell. During an SPR experiment, water was first introduced for at least 6 h for stabilization of the DNC film. Once a flat baseline was obtained, water was replaced by XG solution for 2 h before the water feed was restored for rinsing of any reversibly bound XG from the substrate. Experiments were run in triplicate and results are reported as average surface concentration (Γ_{SPR}) ± one standard deviation.

In SPR experiments, the change in surface plasmon angle θ_{sp} was directly observed and used for calculation of Γ_{SPR} in the unit of mg·m^{-2}, using the equation by de Feijter *et al.*[17]

$$\Gamma_{SPR} = \frac{L(n_a - n_s)}{dn/dc} = \frac{\Delta\theta}{d\theta/dL}\frac{(n_a - n_s)}{dn/dc}$$

in which n_a is the refractive index of the adsorbate (n_a=1.45),[18] n_s is the refractive index of the solvent (n_s=1.33),[19] $d\theta/dL$ is the change in θ_{sp} with the thickness of cellulose film, modeled by the Fresnel equations ($d\theta/dL$=0.043 deg·nm^{-1}),[18] and dn/dc is the refractive index increment. dn/dc=0.137 cm^3·g^{-1}, which Kittle determined by differential refractometry.

3.3.7. Quartz crystal microbalance with dissipation monitoring (QCM-D)

A QCM-D E4 (Q-Sense AB) was employed to detect the "wet mass" of XG adsorbed onto the DNC films. The thickness of each film was first determined by ellipsometry before the sensor crystal was placed into the QCM-D flow module. The flow rate of water and XG solution was set at 0.200 mL·min^{-1} and the temperature of the solutions was 25 °C. During QCM-D experiment, water was first introduced overnight for stabilization of the DNC film. Once a flat baseline was obtained, water was replaced by XG solution for 3 h before the water feed was restored for rinsing of any reversibly bound XG from the substrate. Experiments were run in triplicate and results are reported as average surface concentration (Γ_{QCM}) ± one standard deviation.

In QCM-D experiments, the frequency changes Δf_n at different overtones (n is the overtone) were directly obtained. Additionally, dissipation (D) of the adsorbed layer was observed, which reflects the viscoelastic nature of the adsorbed layer,

$$D = \frac{E_{dissipated}}{2\pi E_{stored}}$$

where $E_{dissipated}$ is the energy dissipated of the quartz due to the viscous nature of the surrounding medium, and E_{stored} is the energy stored in the quartz. An increase in D x 10^6 less than 5% of the

scaled frequency change (Δf_n/n) indicates the adsorbed layer is rigid. The adsorption of XG onto DNC falls in this range, and in this case the Sauerbrey equation can be used to calculate Γ_{QCM} (in the unit mg·m^{-2}) from $\Delta f_n/n$,[20]

$$\Gamma_{QCM} = -C \frac{\Delta f_n}{n}$$

where C is the Sauerbrey constant (0.177 mg·s·m^{-2}). The Sauerbrey equation assumes that the adsorbed layer is rigid and that it has the same shear modulus and density as the quartz.

3.4. Results and discussion

3.4.1. Surface charge density of SNC and DNC

The surface charge densities of SNC and DNC samples were obtained by conductometric titration. The titration curves are shown in Figure 3.1. The titration curve of the SNC sample showed two regions, each of which was fit with a straight line. The equivalence point used for calculating the surface charge density was determined from the intersection of the two linear fits. The initial conductivity of the SNC sample was mainly due to the protons dissociated from the sulfate groups. In contrast, the negatively charged cellulose nanocrystals underwent comparatively slow Brownian motion and therefore contributed little to the total conductivity of the suspension. Once NaOH was added, the protons were neutralized by hydroxyl ions and replaced by less mobile sodium ions, which resulted in a decrease in conductivity. When all protons were neutralized, further continuous addition of NaOH increased the conductivity because it introduced extra hydroxyl and sodium ions.

For the DNC sample, the initial conductivity was very low (~10 μS·cm^{-1}). The conductivity increased monotonically during titration, and no equivalence point was observed.

This indicated that most sulfate groups had been removed in the desulfation process and that the conductometric titration technique was not able to detect any charge in the DNC sample.

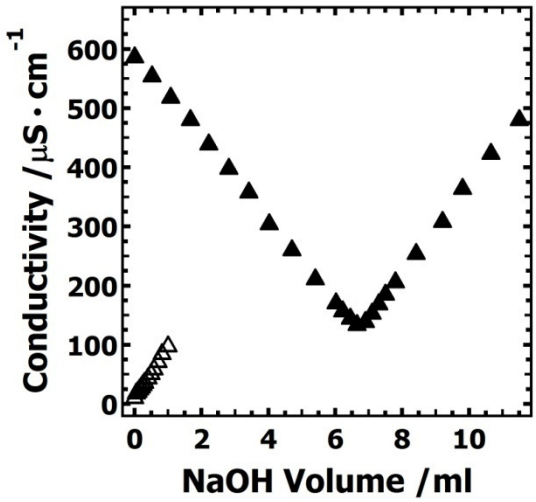

Figure 3.1. Conductometric titration curves for SNC (▲) and DNC (△).

3.4.2. Thicknesses and morphology of DNC films

The DNC film preparation conditions and resulting thicknesses are summarized in Table 3.1. The morphologies of the DNC films, as determined by AFM, are shown in Figure 3.2. For comparison, AFM images of SNC and RC thin films prepared by Kittle are also shown. The root-mean-square roughnesses of the films determined from these images are summarized in Table 3.2. Compared with DNC films, SNC films have a similar morphology but lower roughness. After removal of the negatively charged sulfate groups from the surfaces of the cellulose nanocrystals, the ionic repulsion between cellulose nanocrystals was significantly reduced, resulting in aggregation of the rod-like colloidal particles, which may explain the higher surface roughness of DNC films compared to the SNC films. The amorphous RC films are quite

different from nanocrystalline cellulose films because of their smooth surface (lower roughness) and non porous structure, as reported in the literature.[21]

Table 3.1. Conditions for preparing DNC films with different thicknesses.

DNC suspension concentration (wt%)	Spin coating speed (rpm)	DNC film thickness (nm)
0.3	6000	2.3 ± 0.2
0.4	6000	5.3 ± 0.2
0.5	4000	9.8 ± 0.3
0.75	4000	16.2 ± 0.8
1.0	4000	25.5 ± 0.5
1.1	4000	29.3 ± 0.5
1.2	4000	32.1 ± 0.4

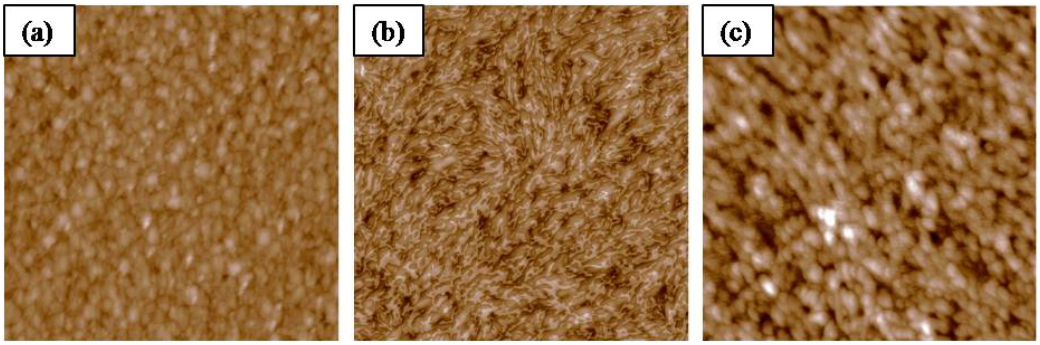

Figure 3.2. AFM height images of cellulose substrates: (a) RC, (b) SNC, and (c) DNC with scan size 2 μm × 2 μm. The z-scale is 20 nm for all images.

Table 3.2. Surface roughnesses of cellulose substrates.

Cellulose substrates	Thickness (nm)	Surface roughness (nm)
DNC	32	3.0 ± 0.1
SNC	25	2.4 ± 0.3
RC	22	1.6 ± 0.1

3.4.3. Dependence of XG adsorption on DNC film thickness

In preliminary SPR adsorption experiments, DNC films with a thickness around 30 nm were exposed to XG solutions with concentrations ranging from 0 to 500 $mg \cdot L^{-1}$. XG adsorption reached equilibrium after 2 h and the amount of irreversibly adsorbed XG did not increase much when the XG concentration was higher than 100 $mg \cdot L^{-1}$. Consequently, an XG exposure time of 2 h and an XG concentration of 100 $mg \cdot L^{-1}$ were adopted for the DNC film thickness dependence study. The dependence of XG surface concentration (Γ) on DNC film thickness (d) was investigated via SPR, as shown in Figure 3.3.

The Γ_{SPR} data show two regimes, a film thickness dependent regime and a thickness independent regime. With d < 25 nm, Γ_{SPR} increases linearly with d. A linear fitting line with a slope of 0.19 ± 0.03 $mg \cdot m^{-2} \cdot nm^{-1}$ is shown in Figure 3.3. With 25 nm < $d \leq$ 33 nm, Γ_{SPR} stays constant at 4.8 ± 0.1 $mg \cdot m^{-2}$. The thickness dependence study on SNC and RC films was completed by Kittle and Edgar and their results are shown in Figure 3.4.[1] Compared with DNC films, SNC films show a similar dependence of XG adsorption on film thickness. Γ_{SPR} also increases linearly with d when d < 10 nm. The slope of the linear fitting line for SNC films is 0.18 ± 0.03 $mg \cdot m^{-2} \cdot nm^{-1}$, almost identical with that of DNC films. When 10 nm < $d \leq$ 27 nm, average Γ_{SPR} = 1.9 ± 0.2 $mg \cdot m^{-2}$. In contrast, for RC films Γ_{SPR} is independent of d.

The two identical slopes in the thickness dependent regions for DNC and SNC films indicate that the negatively charged sulfate groups on the SNC films do not significantly influence XG adsorption. In the thickness independent regions for SNC and DNC (d > 25 nm), at the same thickness, Γ_{SPR} for DNC is more than twice as large as that of SNC. This may be explained as resulting from the larger pore size of the DNC films. According to the study of Jiang *et al.*, fully desulfated cellulose nanocrystals tend to form highly elongated aggregates,[16] which result in a larger pore size, higher film surface roughness, and greater accessible surface area. The thickness dependent regimes on DNC and SNC suggest that XG penetrates into the nanocrystalline cellulose films because of their porous structure. Although when the nanocrystalline cellulose films become thicker (d > 25 nm for DNC and d > 10 nm for SNC), XG is not able to penetrate throughout the entirety of the films. In contrast, the independence of XG adsorption on film thickness and much lower XG surface concentrations observed for RC films are good indications that XG is confined to the surface of the smooth, nonporous RC films. Interestingly, a comparison of the results of the three surfaces shows that "monolayer-thin" cellulose films of DNC, SNC, and RC (~ 2 nm) adsorbed approximately the same amount of XG (Γ_{SPR}~ 0.6 mg·m^{-2}). Nanocrystalline cellulose films (DNC and SNC) exhibit cellulose I crystal structure,[22] while amorphous cellulose films are amorphous.[23] It is reasonable to hypothesize that cellulose morphology and surface charge of the cellulose substrates play a limited role in XG adsorption. Accessible surface areas of the cellulose films may be the factor leading to apparent differences in XG adsorption.

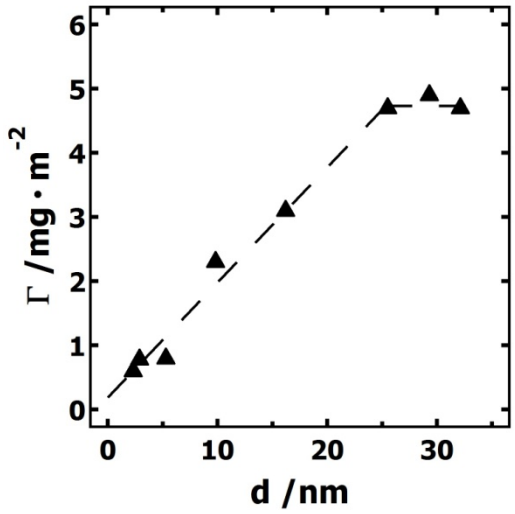

Figure 3.3. Dependence of Γ_{SPR} on film thickness d for XG adsorption onto DNC films (▲,──). Average-value trendlines are for eye guidance.

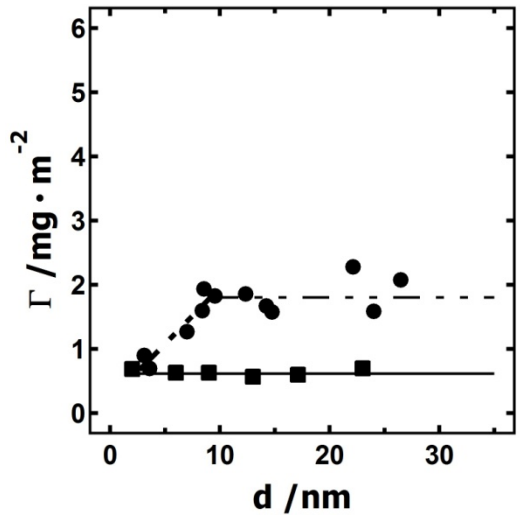

Figure 3.4. Dependence of Γ_{SPR} on film thickness d for XG adsorption onto SNC films (●,----) and RC films (■, ──).Average-value trendlines are for eye guidance.

3.4.4. XG adsorption isotherms

XG adsorption isotherms for DNC thin films (with a thickness of around 30 nm) measured by QCM-D and SPR are shown in Figures 3.5 and 3.6, respectively. Error bars were calculated from measurements made in triplicate. The original data are shown in Appendix A. As seen from Figures 3.5 and 3.6, Γ_{QCM} is greater than Γ_{SPR}. This is expected because SPR only detects the "dry mass" of the adsorbed XG layer,[24] whereas surface concentrations obtained via QCM-D also account for the mass of water trapped in the adsorbed film.[25] Additionally, both adsorption isotherms, from QCM-D and SPR data, were fit with Langmuir and Freundlich isotherms. Because the Freundlich isotherm fit the data more effectively, Langmuir isotherms are not shown in Figures 3.5 and 3.6. The Langmuir and Freundlich isotherms have several key differences. The Langmuir isotherm is described as

$$\Gamma = \frac{\Gamma_m \cdot K_L \cdot C}{1 + K_L \cdot C} \qquad [3.2]$$

where Γ_m is the maximum surface coverage of a single monolayer at infinite bulk concentration, C is the adsorbate bulk concentration, K_L is the Langmuir constant, which is defined as the ratio of the adsorption rate constant (k_{ads}) to the desorption rate constant (k_{des}). The Langmuir model was initially derived from the adsorption of gas molecules onto solid surfaces. It assumes independent, non-preferential binding sites with maximum monolayer coverage (one binding site is occupied by no more than one adsorbate). Although polymer adsorption is usually irreversible and results in multilayers, and therefore differs from gas adsorption, polymer adsorption isotherms may have a similar shape to Langmuir isotherms. When Γ_m exceeds monolayer coverage, the Freundlich isotherm may be applied. In contrast to the Langmuir isotherm, the

Freundlich isotherm assumes heterogeneous surfaces and that the adsorption heat increases exponentially with increasing surface coverage. For Freundlich isotherms,

$$\Gamma = K_F \cdot C^{1/n_f} \qquad [3.3]$$

where K_F is the adsorbent capacity, C is the adsorbate bulk concentration, and $1/n_f$ is the adsorption affinity constant. For XG adsorbed onto DNC films, the Freundlich isotherm parameters were K_F= 3.2 ± 0.1L·mg^{-1} and$1/n_f$= 0.19 ± 0.01 for QCM results and K_F=2.2 ± 0.3 and$1/n_f$= 10.17 ± 0.03for SPR results.

XG adsorption isotherms for SNC thin films (with a thickness of around 13 nm) and RC films (with a thickness of around 15 nm), measured by Kittle and Edgar with QCM-D and SPR,[1] are shown in Figures 3.7 and 3.8, respectively. A comparison of the results obtained for the DNC, SNC, and RC substrates clearly showed that the amount of adsorbed XG decreased in the order DNC > SNC > RC at any given XG concentration. As discussed in the thickness dependence study, this may be attributed to the difference in accessible surface area of the cellulose films.

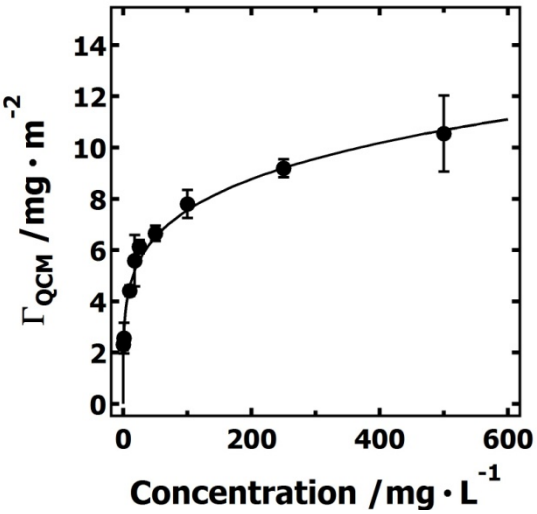

Figure 3.5. Adsorption isotherm of XG onto DNC films via QCM-D (●). Solid line indicates data fit with a Freundlich isotherm.

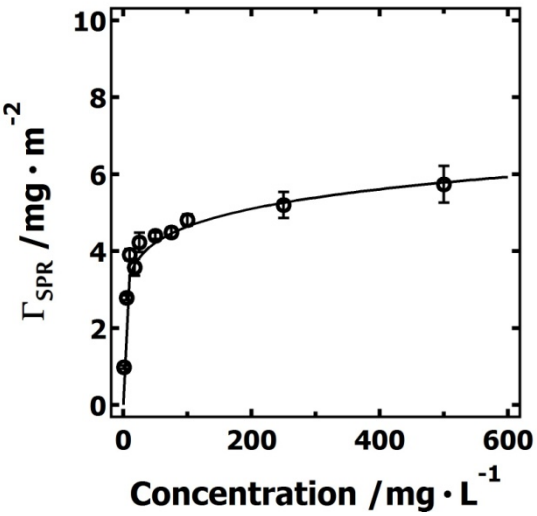

Figure 3.6. Adsorption isotherm of XG onto DNC films via SPR (○). Solid line indicates data fit with Freundlich isotherm.

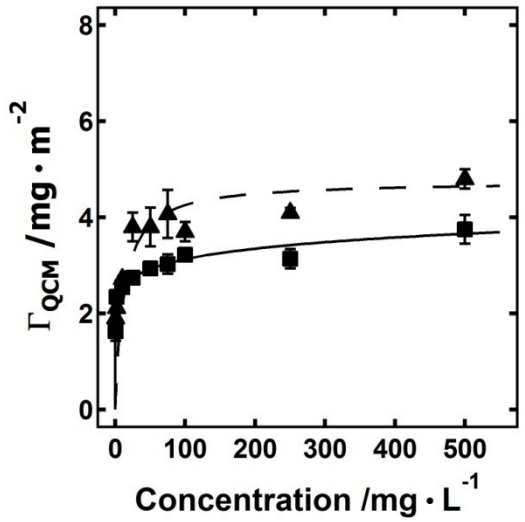

Figure 3.7. Adsorption isotherms of XG onto (▲) SNC and (■) RC films via QCM-D, provided by Kittle and Edgar.[1] Dash line indicates Langmuir isotherm fit. Solid lines indicate Freundlich isotherm fit.

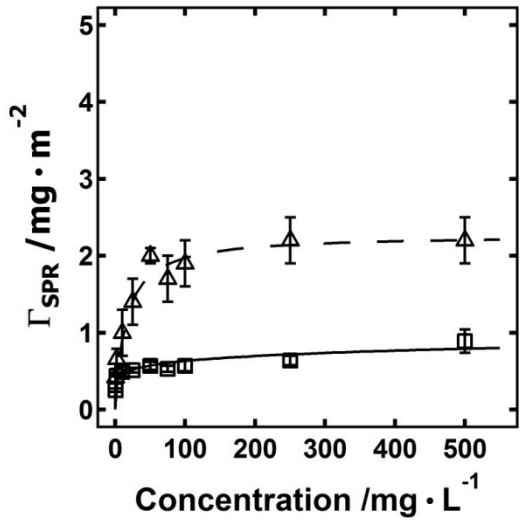

Figure 3.8. Adsorption isotherms of XG adsorbed onto (△) SNC and (□) RC films via SPR, provided by Kittle and Edgar.[1] Dash line indicates Langmuir isotherm fit, solid line indicates Freundlich isotherm fit. For both the QCM-D and SPR experiments, adsorption isotherms for SNC films were well fitted by Langmuir isotherms, whereas adsorption isotherms for the RC films were effectively fitted with Freundlich isotherms. The Freundlich and Langmuir isotherm fitting parameters for the SNC and RC substrates, provided by Kittle and Edgar, are summarized in Table 3.3.[1]

Table 3.3. Freundlich and Langmuir isotherm fitting parameters for XG adsorbed onto RC and SNC films, provided by Kittle and Edgar.[1]

	K_F (L·mg^{-1})		$1/n_f$		Γ_m (mg·m^{-2})		K_L (L·m^{-2})	
	QCM	SPR	QCM	SPR	QCM	SPR	QCM	SPR
RC	2.01 ± 0.07	0.33 ± 0.02	0.10 ± 0.01	0.14 ± 0.02	-	-	-	-
SNC	-	-	-	-	4.8 ± 0.2	2.3 ± 0.2	0.09 ± 0.04	0.07 ± 0.01

3.4.5. Properties of adsorbed XG films

3.4.5.1. Water content and energy dissipation of adsorbed XG films

The water content of the adsorbed XG film is calculated from the difference of Γ_{QCM} and Γ_{SPR},[24]

$$\%water = \left(1 - \frac{\Gamma_{SPR}}{\Gamma_{QCM}}\right) \text{X}100\% \qquad [3.4]$$

Γ_{QCM} and Γ_{SPR} for XG concentrations greater than 2 mg·L^{-1} were collected to calculate the average water content for the adsorbed XG films. The water content for XG films adsorbed onto DNC substrates was 38 ± 5%, which was lower than the water content of adsorbed XG films on SNC and RC substrates (54 ± 9% and 81 ± 3%, respectively, provided by Kittle and Edgar).[1]

In QCM-D experiments, resonant frequency change (Δf) and dissipation factor (D) are obtained simultaneously. The dissipation factor reflects the viscoelastic properties of the adsorbed film and is defined as

$$D = \frac{E_{dissipated}}{2\pi E_{stored}} \qquad [3.5]$$

where $E_{dissipated}$ is the energy dissipated during one period of oscillation due to the viscous nature of the adsorbed film, and E_{stored} is the energy stored in the oscillating system. For XG adsorption onto cellulose films, an increase in ΔD indicates the addition of a more viscous medium to the sensor crystal substrate, whereas a decrease indicates the addition of a more rigid medium. The dissipation changes for XG adsorbed onto DNC films is shown in Figure 3.9. At low concentrations (XG concentration < 250 mg·L^{-1}), ΔD values are negative. The negative ΔD values suggest that after adsorption of XG, the DNC films are more rigid. XG molecules may penetrate the porous DNC films, either excluding water and/or tethering the cellulose

nanocrystals, resulting in a more rigid network. When the XG concentration increases above 250 mg·L^{-1}, the dissipation change increases above zero. A possible explanation could be that after the pores of the DNC film have been saturated with XG, more XG associated with water adsorbs onto the surface of the DNC/XG network and forms a floppy, swollen film, leading to a net increase in dissipation. In comparison, Δ*D* values slightly increased for XG adsorbed onto SNC and RC substrates over XG concentrations ranging from 1 mg·L^{-1} to 500 mg·L^{-1}, indicating that the SNC and RC substrates became less rigid after XG adsorption. This may be due to a higher water content of adsorbed XG films on these substrates.

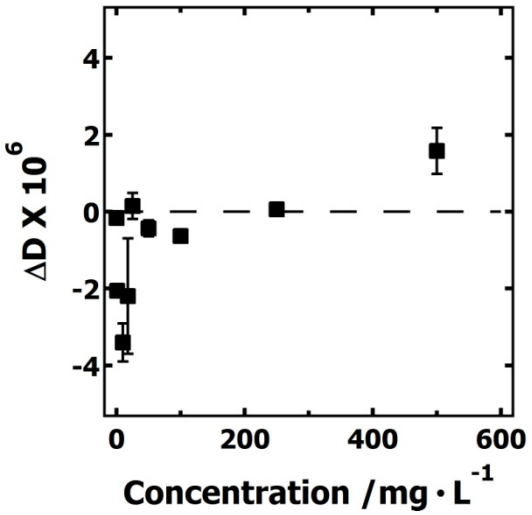

Figure 3.9. Δ*D* (■, 5th overtone) versus concentration for XG adsorbed onto DNC films. The dashed line (—) indicates Δ*D* = 0.

3.4.5.2. AFM images of DNC films before and after XG adsorption

AFM was used to image the morphology of DNC films before and after XG adsorption. DNC surfaces were exposed to both low (10 mg·L^{-1}) and high (500 mg·L^{-1}) concentrations of XG for 3 h, then dried with nitrogen, and immediately imaged with an AFM. The results are shown in Figure 3.10. A bare DNC surface is also shown for reference. It can be observed that

the rod-like DNC nanoparticles lost their features after exposure to XG solutions, and the roughness of DNC films slightly increased from 3.0 ± 0.1 nm (bare surface) to 3.5 ± 0.1 nm (500 $mg \cdot L^{-1}$ XG). The AFM images of SNC and RC substrates are shown in Figure 3.11 for comparison. The roughness of the SNC films remained almost the same (~ 2.4 nm) before and after XG adsorption. In contrast, RC films that had been exposed to 500 $mg \cdot L^{-1}$ XG showed spherical XG aggregates, although XG aggregates covered less than 10% of the total surface area. The roughness of the RC substrates increased from 1.56 ± 0.01 nm to 3.8 ± 0.9 nm upon exposure. Line scan analyses indicated the height of XG aggregates was between 10 and 20 nm., as the R_g of XG (~ 120 kDa) in solution is about 120 nm,[26] XG adsorbed onto RC films in a flatter confirmation. Again, these results indicate that because of the porous structure of the nanocrystalline cellulose films, XG molecules could penetrate into the pores of DNC/SNC films. The XG molecules confined to the surface on the RC films, forming floppy aggregates with a high water content.

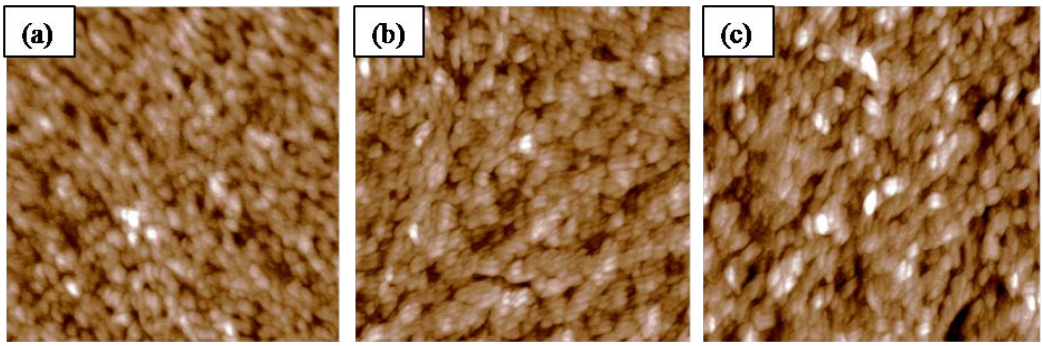

Figure 3.10. AFM height images of DNC substrates: (a) bare DNC film, (b) DNC film exposed to10 $mg \cdot L^{-1}$ XG, (c) DNC film exposed to 500 $mg \cdot L^{-1}$ XG. The scan size and z-scale are 2μm × 2 μm and 20 nm, respectively, for all images.

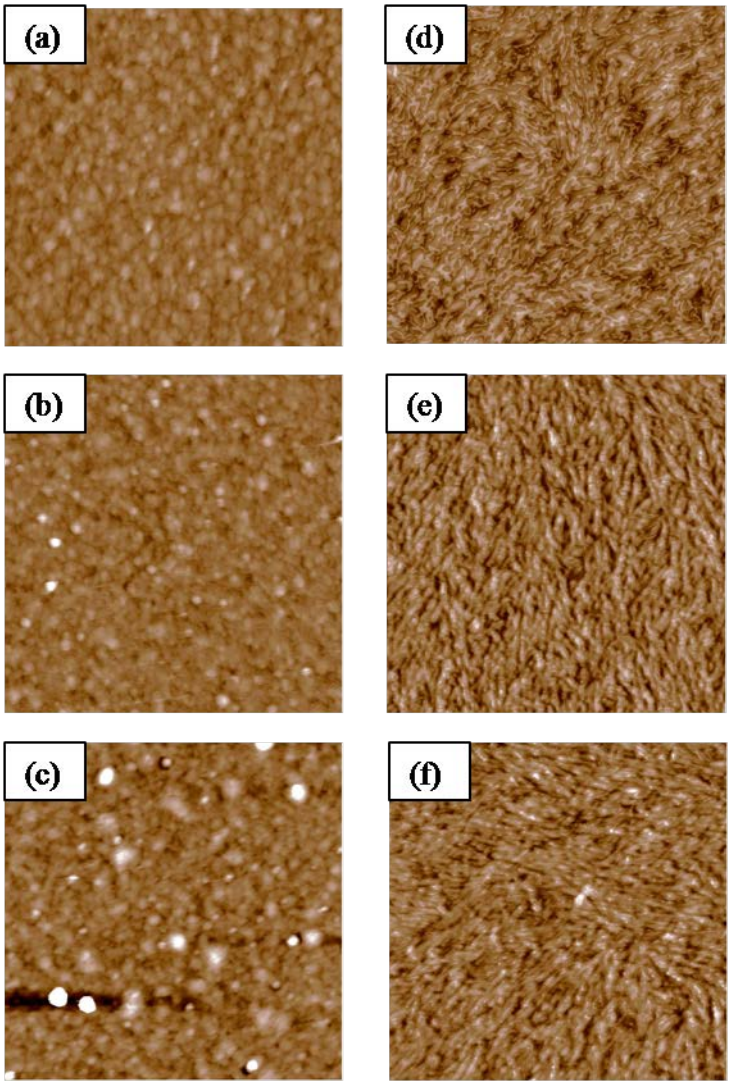

Figure 3.11. AFM height images of RC and SNC substrates: (a) bare RC film, (b) RC film exposed to 10 mg·L^{-1} XG, (c) RC film exposed to 500 mg·L^{-1} XG, (d) bare SNC film, (e) SNC film exposed to 10 mg·L^{-1} XG, and (f) SNC film exposed to 500 mg·L^{-1} XG. The scan size and z-scale are 2μm × 2 μm and 20 nm, respectively, for all images.

Based on the combined results from the studies of the film thickness dependence of XG adsorption, the XG adsorption isotherms, and the properties of adsorbed XG films, a model for XG adsorption onto DNC, SNC, and RC films is proposed in Figure 3.12. XG partially

penetrates into both DNC and SNC films because of their porous structure. In DNC films, XG excludes water and/or tethers the rod-like nanocrystals to form a rigid network. If the concentration of XG is high enough, more XG adsorbs onto the film surface after saturating the internal pores. The adsorption mechanism of XG on SNC films is quite similar to that on DNC films. However, XG penetrates less deeply into the films because of the smaller pore size of SNC films compared to DNC films. On RC films, XG adsorption is driven by hydrogen bonding, and most adsorbed XG is confined to the film surface, forming a viscous, floppy layer with a high water content.

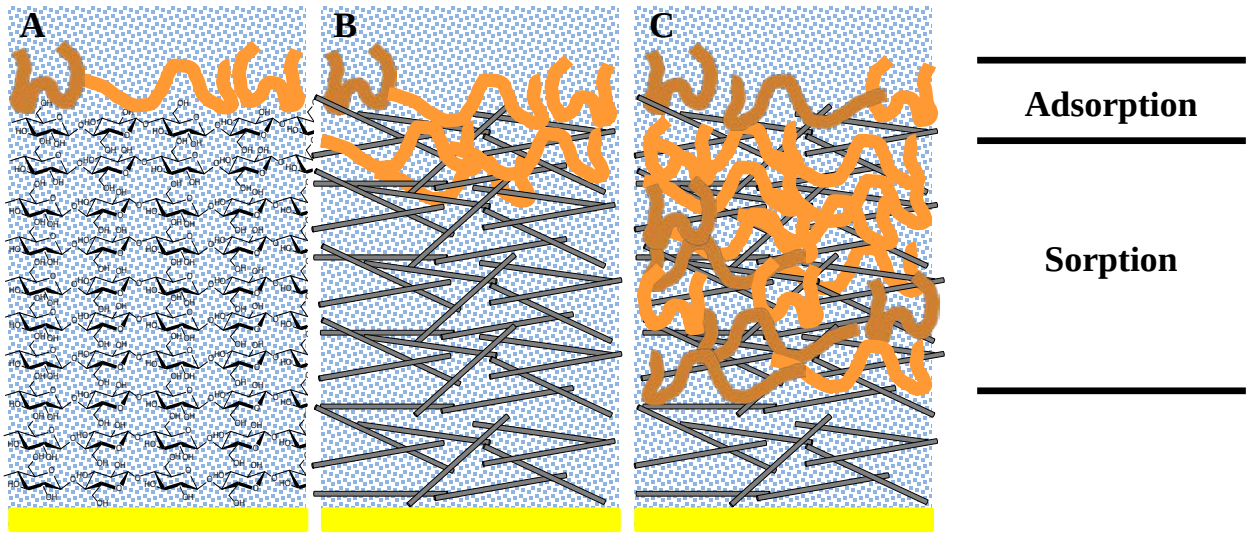

Figure 3.12. Schematic illustration of XG adsorption onto (A) RC films, (B) SNC films, and (C) DNC films.

3.5. Conclusions

In this study, the amount of XG that adsorbed onto cellulose films from DNC, SNC, and RC decreased in the order DNC > SNC > RC. XG adsorption on DNC films was strongly

dependent upon film thickness whereas it was weakly dependent upon film thickness for SNC films. However, "monolayer-thin" films of DNC, SNC, and RC adsorbed approximately the same amount of XG. These results suggest that cellulose morphology and surface charge of the cellulose substrate play a limited role in XG adsorption and that accessible surface area of the cellulose film may be the factor leading to apparent differences in XG adsorption for different surfaces.

3.6. Acknowledgements

This project was supported in part by the Center for LignoCellulose Structure and Formation, an Energy Frontier Research Center funded by the U.S. Department of Energy, Office of Science, Office of Basic Energy Sciences under Award Number DE-SC0001090. The project was also partially supported by the National Science Foundation (CHE-0724126), the Macromolecules and Interfaces Institute at Virginia Tech, and the U.S. Department of Transportation through the Southeastern Sun Grant Center.

3.7. References

(1) Kittle, J. D.; Edgar, E. jokittle@vt.edu (Kittle), edgaem7@gmail.com (Edgar).

(2) Reiter, W.-D. *Curr. Opin. Plant Biol.* **2002**, *5*, 536.

(3) Cosgrove, D. J. *Nat. Rev. Mol. Cell Biol.* **2005**, *6*, 850.

(4) Himmel, M. E.; Ding, S.-Y.; Johnson, D. K.; Adney, W. S.; Nimlos, M. R.; Brady, J. W.; Foust, T. D. *Science (Washington, DC, U. S.)* **2007**, *315*, 804.

(5) Ragauskas, A. J.; Williams, C. K.; Davison, B. H.; Britovsek, G.; Cairney, J.; Eckert, C. A.; Frederick, W. J., Jr.; Hallett, J. P.; Leak, D. J.; Liotta, C. L.; Mielenz, J. R.; Murphy, R.; Templer, R.; Tschaplinski, T. *Science (Washington, DC, U. S.)* **2006**, *311*, 484.

(6) Albersheim, P. D., A.; Roberts, K.; Sederoff, R.; Staehelin, A. *Plant Cell Wall: from Chemistry to Biology*; Garland Science: New York, 2011.

(7) Jarvis, M. C. *Food Hydrocolloids* **2010**, *25*, 257.

(8) Hayashi, T. *Annu. Rev. Plant Physiol. Plant Mol. Biol.* **1989**, *40*, 139.

(9) Brumer, H.; Zhou, Q.; Baumann, M. J.; Carlsson, K.; Teeri, T. T. *J. Am. Chem. Soc.* **2004**, *126*, 5715.

(10) Ahola, S. *Bioresources* **2008**, *3*, 1315.

(11) Lopez, M.; Bizot, H.; Chambat, G.; Marais, M.-F.; Zykwinska, A.; Ralet, M.-C.; Driguez, H.; Buleon, A. *Biomacromolecules* **2010**, *11*, 1417.

(12) Vincken, J. *Plant physiology (Bethesda)* **1995**, *108*, 1579.

(13) Bodin, A.; Ahrenstedt, L.; Fink, H.; Brumer, H.; Risberg, B.; Gatenholm, P. *Biomacromolecules* **2007**, *8*, 3697.

(14) Hayashi, T.; Marsden, M. P. F.; Delmer, D. P. *Plant Physiol.* **1987**, *83*, 384.

(15) Revol, J. F.; Bradford, H.; Giasson, J.; Marchessault, R. H.; Gray, D. G. *Int. J. Biol. Macromol.* **1992**, *14*, 170.

(16) Jiang, F.; Esker, A. R.; Roman, M. *Langmuir* **2010**, *26*, 17919.

(17) De, F. J. A.; Benjamins, J.; Veer, F. A. *Biopolymers* **1978**, *17*, 1759.

(18) Kaya, A.; Du, X.; Liu, Z.; Lu, J. W.; Morris, J. R.; Glasser, W. G.; Heinze, T.; Esker, A. R. *Biomacromolecules* **2009**, *10*, 2451.

(19) Zwolinski, B. J.; Eicher, L. D. *J. Phys. Chem.* **1971**, *75*, 2016.

(20) Sauerbrey, G. *Z. Phys.* **1959**, *155*, 206.

(21) Kontturi, E.; Thüne, P. C.; Niemantsverdriet, J. W. *Langmuir* **2003**, *19*, 5735.

(22) Jiang, F., Virginia Polytechnic Institute and State University, 2011.

(23) Kontturi, E.; Suchy, M.; Penttilä, P.; Jean, B.; Pirkkalainen, K.; Torkkeli, M.; Serimaa, R. *Biomacromolecules* **2011**, *12*, 770.

(24) Hedin, J.; Loefroth, J.-E.; Nyden, M. *Langmuir* **2007**, *23*, 6148.

(25) Kanazawa, K. K.; Gordon, J. G., II *Anal. Chem.* **1985**, *57*, 1770.

(26) Xu, H.; Schlenoff, J. B. *Langmuir* **1994**, *10*, 241.

CHAPTER 4

Effects of non-ionic surfactant Tween 80 on the adsorption of cellulase onto self-assembled monolayers

4.1. Abstract

Residual lignin present in pretreated lignocellulosic biomass is believed to hinder its enzymatic hydrolysis by inactivating the cellulase enzymes through irreversible adsorption. Non-ionic surfactants have been shown to prevent non-productive cellulase adsorption and enhance the yield of enzymatic hydrolysis. However, the interactions between cellulase and the functional groups of lignin, as well as the effects of non-ionic surfactants on these interactions are not well understood. This study investigates the adsorption of cellulase on untreated and Tween 80-treated self assembled monolayers (SAMs) with selected functional groups found in lignin (–CH_3, –OH and –COOH). Cellulase adsorption was monitored by quartz crystal microbalance with dissipation monitoring and surface plasmon resonance. The morphology of the adsorbed cellulase layer was analyzed by atomic force microscopy. Large amounts of cellulase adsorbed onto SAM-CH_3 and SAM-COOH substrates, where adsorption is most likely driven by hydrophobic and electrostatic interactions, respectively. However, cellulase adsorption onto SAM-OH substrates, which is mainly driven by hydrogen bonding, was limited. Tween 80 adsorbed onto the hydrophobic SAM-CH_3 substrates and hindered the adsorption of cellulase. However, the interactions between Tween 80 and SAM-OH and SAM-COOH were weak so that

Tween 80 adsorbed only reversibly and had no effect on the adsorption of cellulase on SAM-OH and SAM-COOH.

4.2. Introduction

Uncertainty in the supply of petroleum resources and concerns about the environmental consequences of fossil fuel consumption lead to the development of sustainable alternative energy.[1] Renewable fuels derived from lignocellulosic biomass, such as agricultural and forestry residuals and industrial wastes, offer economic and environmentally benign energy, and are thus attracting increasing research interest as a promising substitute for traditional petroleum.[1-3] The bioconversion of lignocellulosic biomass to bioethanol usually involves three steps: biomass pretreatment, enzymatic hydrolysis, and fermentation.[4] The pretreatment process breaks up the recalcitrant lignin matrix and isolates cellulosic materials for subsequent enzymatic hydrolysis. Cellulose and hemicelluloses are converted into simple sugars by cellulase in the enzymatic hydrolysis step. In the fermentation step, bioethanol is produced from these sugars. The pretreatment and enzymatic hydrolysis are the most costly steps and are considered the economic barrier for producing bioethanol on an industrial scale.[5-7] Residual lignin in these two steps has been shown to act as a cellulase inhibitor. In plant cell walls, lignin binds to cellulose and hemicelluloses, thus providing mechanical strength and moisture resistance to the lignocellulosic structure. It causes steric hindrance and limits the accessibility of cellulosic enzymes to cellulose materials. Additionally, cellulase will non-specifically adsorb onto lignin and become inactive during hydrolysis.[3-4,8-10] Understanding the mechanism of cellulase adsorption onto lignin is of critical importance for optimizing the production of cellulosic biofuels.

In his PhD research, Dr. Feng Jiang, a former student in Prof. Roman's lab, analyzed the functional group distributions of kraft lignin, organosolv lignin, and milled wood lignin by nuclear magnetic resonance (NMR) spectroscopy. He prepared lignin model surfaces from three lignins and studied the adsorption of cellulase derived from *Trichoderma reesei* onto these model surfaces. Jiang's results indicated that the adsorption of cellulase was driven by both hydrophobic and polar interactions, depending upon the chemical properties of the lignin.[11] Berlin *et al.* selected seven cellulases and investigated the inhibition of cellulase activity by organosolv pretreated softwood lignin with controlled particle size and surface area.[4] Their work also showed that hydrophobic interactions were important for cellulase adsorption. However, whether the presence of carboxyl and hydroxyl groups on lignin surfaces plays a role in cellulase adsorption remains unclear. It is therefore necessary to investigate the interactions between cellulase and various functional groups of lignin, which provide important information for understanding the mechanism of cellulase adsorption onto lignin.

Non-ionic surfactants have been studied as additives that can enhance the effectiveness of cellulase and increase enzymatic hydrolysis yields.[12-14] For example, Tween 80 (polyoxyethylene (20) sorbitan monooleate) has been reported to increase the enzymatic hydrolysis rate of newspaper cellulose by 33%.[12] It is believed that non-ionic surfactants prevent non-productive adsorption of cellulase onto lignin.[13,15-17] In his dissertation, Jiang showed that Tween 80, adsorbed onto a lignin surface and reduced the adsorption of cellulase onto lignin *via* hydrophobic interactions. Additionally, Tween 80 may remove some lignin molecules from the substrate. However, it is still ambiguous how Tween 80 influences the interactions between cellulase and the functional groups of lignin.

In this study, methyl, hydroxyl and carboxyl terminated self-assembled monolayers (SAMs) were prepared on gold substrates. By investigating the adsorption of cellulase on untreated SAMs *via* quartz crystal microbalance with dissipation monitoring (QCM-D), surface plasmon resonance (SPR), and atomic force microscopy (AFM), the interactions between cellulase and individual functional groups of lignin were elucidated. Tween 80-treated SAMs were employed to study the effect of the non-ionic surfactant on the interactions between cellulase and the functional groups mentioned above. The purpose of this study is to better understand the interactions between cellulolytic enzymes and lignin and the effect of non-ionic surfactants on these interactions on a molecular basis.

4.3. Experimental section

4.3.1. Materials

Tween 80 (SigmaUltra), Celluclast 1.5 L (cellulase solution derived from *T. reesei,* Novozyme), 1-dodecanethiol (98%), 11-mercapto-1-undecanol (99%) and 12-mercapto-dodecanoic acid (96%) were purchased from Sigma-Aldrich. Citric acid monohydrate (Certified ACS), sodium hydroxide (Acros Organics, 98.5%), hydrogen peroxide (34-37%, Technical Grade), sulfuric acid (95.9 wt%, Certified ACS Plus) and ethanol (200 proof, Decon labs, Inc) were purchased from Fisher Scientific. All water used was deionized (DI) water with a resistivity of 18.2 MΩ·cm, obtained from a Millipore Direct-Q 5 Ultrapure Water System.

4.3.2. Preparation and characterization of self-assembled monolayers (SAMs)

Gold QCM-D (Q-sense AB, gold, 5 MHz) and SPR (Reichert, gold) sensor chips were cleaned by exposure of the gold surface to piranha solution (7:3 (v/v) mixture of sulfuric acid and

hydrogen peroxide) for 40 min, rinsed with DI water and dried in a stream of nitrogen. Immediately upon drying, the sensor slides were placed in a 1 mM solution of thiol (1-dodecanethiol, 11-mercapto-1-undecanol, or 12-mercaptododecanoic acid) in ethanol for at least 24 hours. When they were needed, the SAM substrates were retrieved from the thiol solution, rinsed with ethanol for the removal of excess thiol molecules, rinsed with DI water, dried in a stream of nitrogen, and immediately characterized in terms of contact angle and surface roughness. The contact angles of the SAM substrates were determined from sessile drop contact angles, measured with a video-based contact angle goniometer (FTA200, First Ten Angstroms, Inc.). 1-dodecanethiol-treated gold substrates (SAM-CH_3) had a contact angle of 102±5°. In contrast, gold substrates treated with 11-mercapto-1-undecanol (SAM-OH) and 12-mercaptododecanoic acid (SAM-COOH) had contact angles of 9.6±1.5° and 6.1±1.0°, respectively. According to the literature, the contact angles for SAM-CH, SAM-OH and SAM-COOH are 114.1±0.4°, 8.6±2.4° and 4.3±1.2°.[18] So the contact angles measured were reasonably close to the values reported by the literature. As expected, the contact angle results indicated that the SAM-CH_3 substrates were hydrophobic, whereas the SAM-OH and SAM-COOH substrates were hydrophilic. The surface roughnesses of the SAMs will be reported in section 4.4.3.

4.3.3. Monitoring adsorption by quartz crystal microbalance with dissipation monitoring (QCM-D)

A 1 M sodium citrate buffer (pH=4.5) was prepared by dissolution of a predetermined amount of citric acid monohydrate and sodium hydroxide in DI water. 1 mM Tween 80 solution, used in the experiments, was prepared by mixing of 2 mL of 50 mM Tween 80 solution in DI water with 5 mL of 1 M sodium citrate buffer, followed by dilution with DI water to 100 mL. 50 mM sodium citrate buffer solution (pH=4.8) was prepared by twenty fold dilution of 1 M sodium

citrate buffer 20 times by volume with DI water. In the remainder of this chapter, the term buffer solution refers to 50 mM sodium citrate buffer. Cellulase solution was prepared by dilution of 0.5 g Celluclast 1.5 L with 100 mL buffer solution.

A Q-Sense E4 QCM-D system was used for measurement of the "wet mass" of cellulase adsorbed on the SAMs. The flow rate for all solutions was set at 0.25 $mL \cdot min^{-1}$ and the temperature of the solutions was 22.00 ± 0.02 °C. The contact angles of the SAM substrates were determined before the slides were placed into the QCM-D flow modules. For measurements of cellulase adsorption onto untreated SAMs, an initial buffer solution was introduced until a flat baseline was obtained, upon which it was switched to cellulase solution. After 40 min of cellulase adsorption, the buffer feed was restored for removal of reversibly adsorbed cellulase from the SAM. For measurements of cellulase adsorption on Tween 80-treated SAMs, once the flat based line was obtained, the initial buffer solution was replaced by 1 mM Tween 80 solution for 23 min. Then, the buffer solution was restored for 20 min for rinsing of loosely bound Tween 80 molecules off of the substrates. Finally, a 40 min cellulase solution feed was introduced for cellulase adsorption, followed by a buffer rinse. In QCM-D experiment, the scaled frequency change of the fifth overtone, ($\Delta f_5/5$), was used for the calculation of surface concentration (Γ_{QCM}) in units of $mg \cdot m^{-2}$.

4.3.4. Monitoring adsorption by surface plasmon resonance (SPR)

A Reichert SR7000 SPR spectrometer was used for measurement of the "dry mass" (or "optical mass") of cellulase adsorbed onto the SAMs. The flow rate for all solutions was set at 0.25 $mL \cdot min^{-1}$ and the temperature of the solutions was 22.00 ± 0.02 °C. The contact angles of the SAM substrates were determined before the slides were placed into the SPR flow modules. The buffer, Tween 80, and cellulase solutions used in SPR experiments were the same as the

solutions used in QCM-D experiments. All solutions were degassed for at least 8 h before being introduced into the flow cell. A switch valve was used to switch solution feeds and care was taken when switching solutions to avoid introducing bubbles into the flow cell. Measurements of cellulase adsorption were carried out in the same manner as the QCM-D experiments. The change in surface plasmon resonance angle, θ_{sp}, was recorded and used for the calculation of surface concentration (Γ_{SPR}) in units of mg·m^{-2}. Equations used for calculating Γ_{SPR} are provided in the literature review chapter (equations 2.8 to 2.12).

4.3.5. Atomic force microscopy (AFM)

An Asylum Research AFM (MFP-3D-BIO, Asylum Research) was used for AFM imaging. During AFM measurements, height images were obtained under ambient conditions (22 °C, 50% humidity) with OMCL-AC160TS standard silicon probes (Olympus Corp.). The roughness of height images was determined with the MFP-3D software as the root mean square value of all collected height values in the scanned area.

4.4. Results and discussion

4.4.1. Adsorption of cellulase onto untreated SAMs

4.4.1.1. Surface concentration of cellulase determined by QCM-D and SPR

Cellulase adsorption onto untreated SAM-CH_3, SAM-OH, and SAM-COOH substrates was first monitored by QCM-D. The results are shown in Figure 4.1. Dissipation changes indicated that cellulase formed rigid layers on all three SAMs, so that the Sauerbrey equation could be used to calculate the surface concentration Γ_{QCM}. However, both adsorbed cellulase and water molecules trapped in the adsorbed cellulase layer contribute to Γ_{QCM} because of the working mechanism of

QCM-D. Thus, SPR was used in addition to obtain the surface concentration Γ_{SPR}, which excludes the influence of water. SPR results are shown in Figure 4.2. Γ_{QCM} and Γ_{SPR} values are listed in Table 4.1. Both QCM-D and SPR results suggest much larger amounts of cellulase irreversibly adsorbed on SAM-CH_3 and SAM-COOH compared to SAM-OH. For SAM-CH_3 substrates, cellulase adsorption occurred most likely *via* hydrophobic interactions.[19-21] For SAMs formed by 11-mercaptododecanoic acid, the reported pKa = 4.8-5.5.[22-23] It is reasonable to assume SAMs prepared from 12-mercaptododecanoic acid have pKa values around 5.0. Consequently, in the sodium citrate buffer (pH = 5.0), about half of the carboxyl groups of the SAM-COOH substrates were dissociated into $-COO^-$ groups, resulting in negative charges on SAM-COOH. Celluclast 1.5 L is a mixture of *T. reesei* cellulase enzymes. Using electrostatic potential maps for the catalytic domains of two of these enzymes (CBH I and EG I), Jiang showed that although the electrostatic potential was predominantly negative, a few spots exhibited positive electrostatic potential,[11] which may be due to positively charged amino groups on the enzymes. During adsorption onto SAM-COOH substrates, conformational changes in the enzymes, exposing their positively charged parts, may result in attractive electrostatic interactions with the negatively charged substrates. In contrast to SAM-COOH and SAM-CH_3 substrates, very little cellulase adsorbed onto SAM-OH substrates, indicating that hydrogen bonding plays only a minor role in the adsorption of cellulase onto solid substrates.

4.4.1.2. Water content of adsorbed cellulase layers

The water contents of the adsorbed cellulase layers were calculated from the difference of Γ_{QCM} and Γ_{SPR},[24] and listed in Table 4.1.

$$\%\,water = \left(1 - \frac{\Gamma_{SPR}}{\Gamma_{QCM}}\right) \text{X}100\% \qquad [4.1]$$

Cellulase adsorbed onto SAM-CH_3 had the lowest water content. This result is not surprising because the SAM-CH_3 substrates are hydrophobic, and cellulase adsorption onto the SAM-CH_3 was driven by interactions with non-polar amino acid residues, resulting in the exclusion of water from the cellulase layer. The water contents between cellulase adsorbed onto SAM-COOH and SAM-CH_3 were not statistically different, suggesting enzymes may form a rigid monolayer on SAM-COOH. Compared to that on SAM-CH_3 and SAM-COOH, cellulase adsorbed onto the hydrophilic SAM-OH substrates had a higher water content, which indicates cellulase adsorbed onto the SAM-OH as floppy aggregates and maintained their 3-D structure like they have in the aqueous state. This interpretation agrees with the dissipation change observed during the QCM-D experiments, in which cellulase adsorbed onto SAM-OH had a greater dissipation increase compared with adsorption onto the SAM-CH_3 and SAM-COOH surfaces.

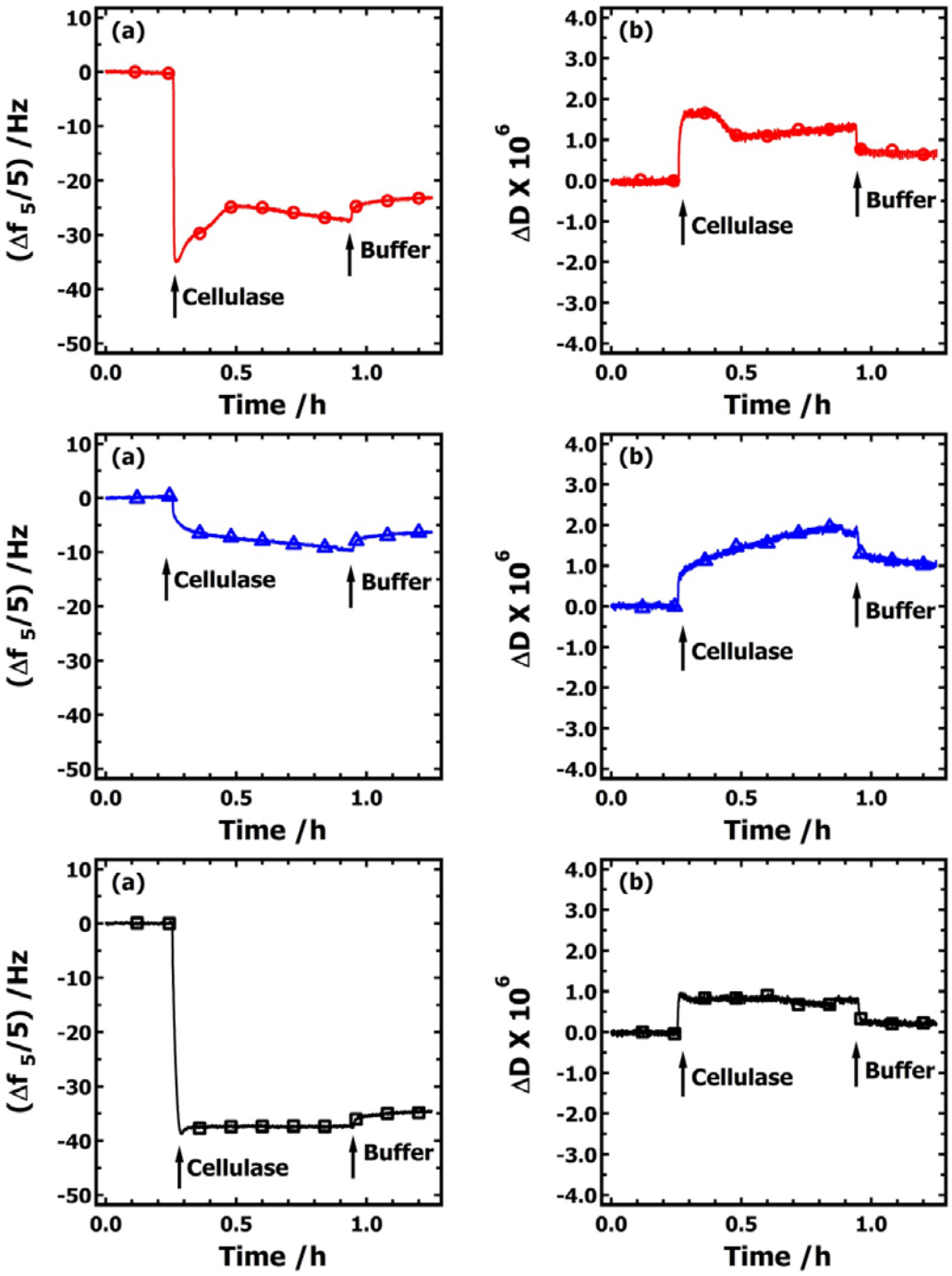

Figure 4.1. (a) Scaled frequency change ($\Delta f_5/5$) and (b) dissipation change (ΔD) (5^{th} overtone) during cellulase adsorption onto untreated SAMs: SAM-CH_3 (red ○), SAM-OH (blue △), and SAM-COOH (black □). Arrows indicate switching of the liquid feed during the experiment.

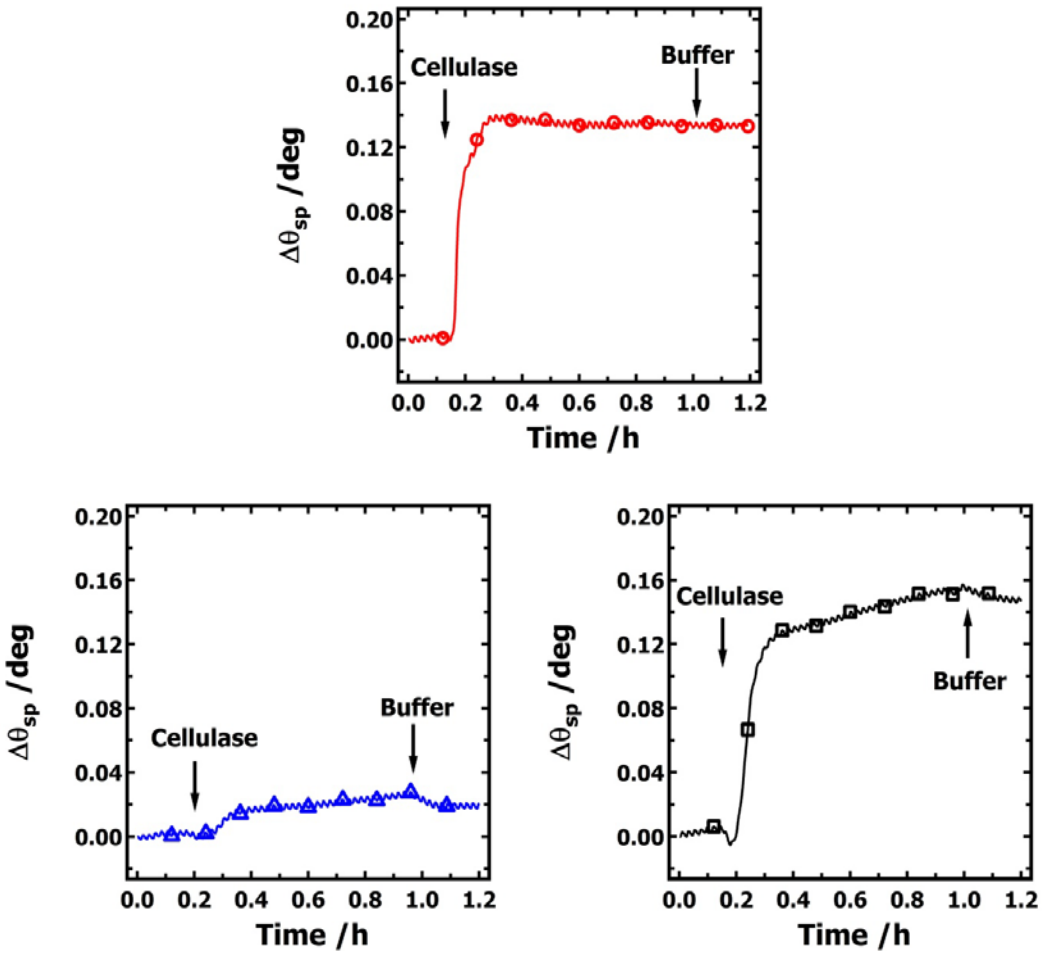

Figure 4.2. $\Delta\theta_{sp}$ versus time during cellulase adsorption onto untreated SAMs: SAM-CH_3 (red ○), SAM-OH (blue △), and SAM-COOH (black □). Arrows indicate switching of the liquid feed during the experiment.

Table 4.1. Surface concentrations, Γ_{QCM} and Γ_{SPR}, and water contents of the adsorbed cellulase layers on the SAM substrates.

Substrate	Γ_{QCM} (mg·m^{-2})	Γ_{SPR} (mg·m^{-2})	Water content (%)
SAM-CH_3	4.2 ± 0.2	2.1 ± 0.3	49 ± 6
SAM-OH	1.2 ± 0.1	0.33 ± 0.03	72 ± 9
SAM-COOH	6.2 ± 0.2	2.8 ± 0.3	55 ± 7

4.4.2. Adsorption of cellulase onto Tween 80-treated SAMs

Cellulase adsorption onto Tween 80-treated SAM-CH_3, SAM-OH, and SAM-COOH substrates was monitored by both SPR and QCM-D. The results are shown in Figures 4.3 and 4.4, respectively. Data obtained from the two techniques agree well. Surface concentrations listed in Table 4.2 are calculated from SPR experiments. The surface concentration of irreversibly adsorbed Tween 80 ($\Gamma_{Tween\ 80\_irr}$) is calculated from the increase of θ_{sp} between t=0.2 h and t=1.2 h. The total surface concentration of cellulase adsorbed onto Tween 80-treated SAMs ($\Gamma_{cellulase\_tot}$), includes both reversible adsorption and irreversible adsorption. $\Gamma_{cellulase\_tot}$ is calculated from the increase of θ_{sp} between t=1.3 h and t=2.2 h of the experiment. The surface concentration of cellulase after the surface is rinsed with buffer ($\Gamma_{cellulase\_irr}$), is calculated from the increase of θ_{sp} between t=2.2 h and t=2.4 h. For SAM-CH_3, a considerable amount of Tween 80 adsorbed onto the substrates and Tween 80 adsorption was mostly irreversible. A possible explanation is that the amphiphilic Tween 80 molecules, comprised of a hydrophobic tail and a branched hydrophilic head group, likely interacted with the SAM-CH_3 substrates through the hydrophobic tails *via* van der Waals interactions, exposing their hydrophilic head groups to the liquid medium. The hydrophobic interactions between Tween 80 and SAM-CH_3 substrates were strong enough to prevent Tween 80 removal from the surface during the buffer rinsing step. After switching the flow feed to cellulase solution, instead of observing an increase in θ_{sp} due to cellulase adsorption, it seems the system experienced a slight mass loss. The possibilities are either cellulase interacted with Tween 80 and led to the desorption of some Tween 80, or a limited amount of cellulase exchanged with Tween 80 at the SAM-CH_3 surface (cellulase adsorption and Tween 80 desorption occurred at the same time).

For the hydrophilic SAM-OH and SAM-COOH substrates, adsorption of Tween 80 was mostly reversible. This result suggests interactions, such as hydrogen bonding, between the hydrophilic head group of Tween 80 and the hydrophilic surfaces are too weak to overcome the entropic penalty for macromolecule immobilization at the surface. From these results it can be concluded that Tween 80 significantly hindered the adsorption of cellulase onto SAM-CH_3 substrates but had almost no effect on the adsorption of cellulase onto SAM-OH and SAM-COOH substrates.

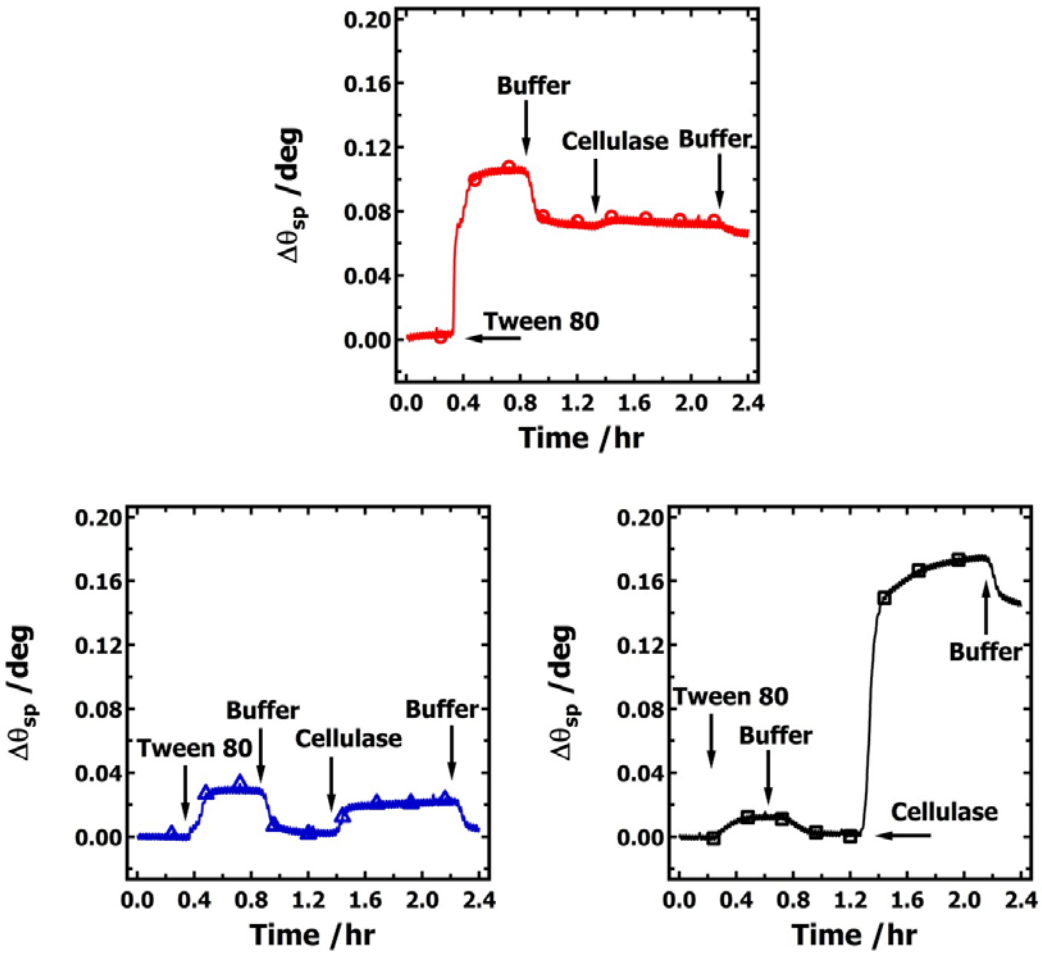

Figure 4.3. $\Delta\theta_{sp}$ versus time during cellulase adsorption onto Tween 80-treated SAMs: SAM-CH_3 (red ○), SAM-OH (blue △), and SAM-COOH (black □). Arrows indicate switching of the liquid feed during the experiment.

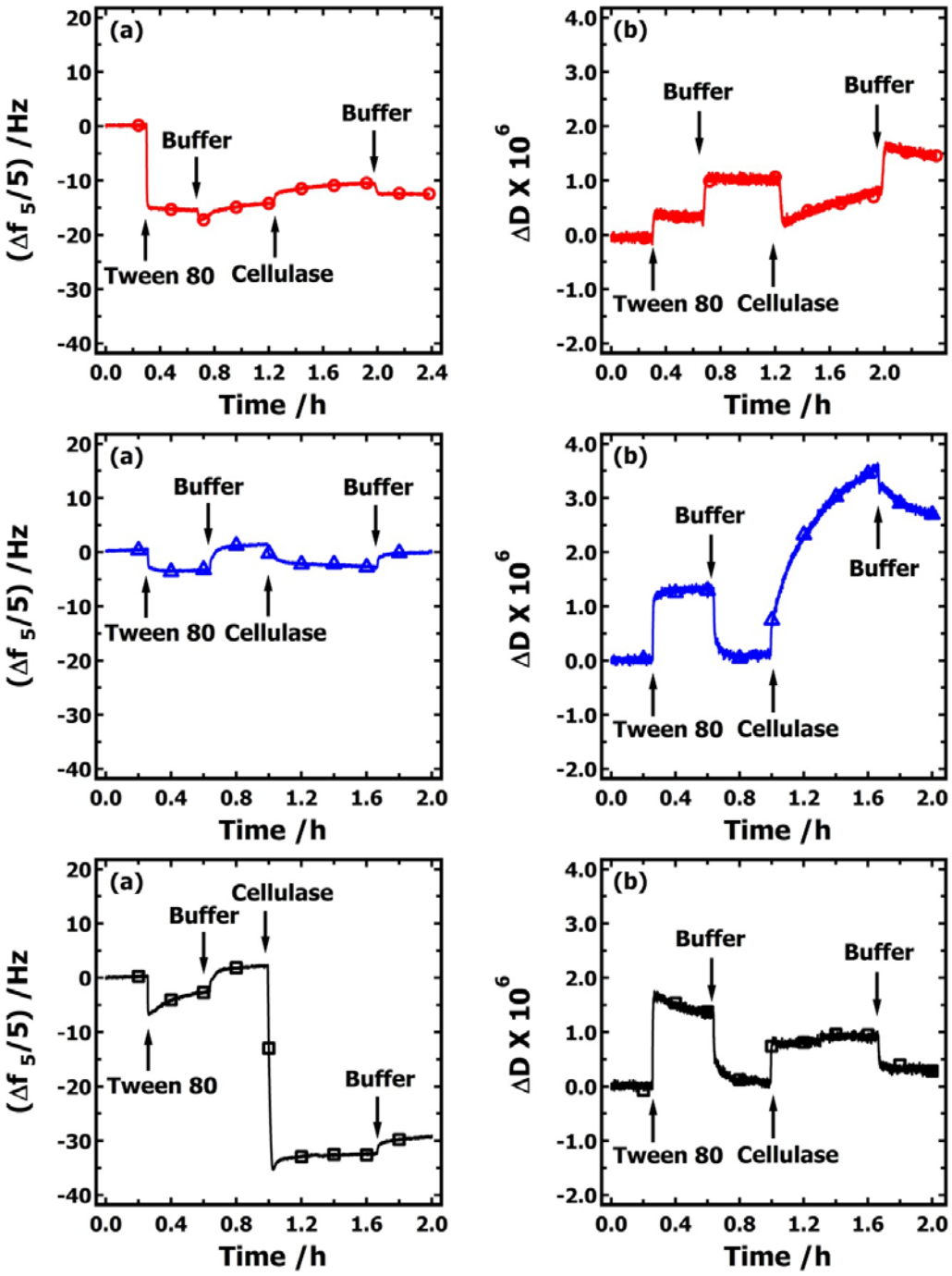

Figure 4.4. (a) Scaled frequency change ($\Delta f_5/5$) and (b) dissipation change (ΔD) (5^{th} overtone) during cellulase adsorption onto Tween 80-treated SAMs: SAM-CH_3 (red ○), SAM-OH (blue △), and SAM-COOH (black □). Arrows indicate switching of the liquid feed during the experiment.

Table 4.2. Surface concentrations from SPR of adsorbed Tween 80 ($\Gamma_{Tween\ 80\_irr}$) and cellulase ($\Gamma_{cellulase\_tot}$, $\Gamma_{cellulase\_irr}$) adsorbed onto SAM substrates.

Substrate	$\Gamma_{Tween\ 80\_irr}$ (mg·m^{-2})	$\Gamma_{cellulase\_tot}$ (mg·m^{-2})	$\Gamma_{cellulase\_irr}$ (mg·m^{-2})
SAM-CH_3	1.38 ± 0.35	0.036 ± 0.001	-0.03 ± 0.02
SAM-OH	0.08 ± 0.04	0.50 ± 0.15	0.05 ± 0.01
SAM-COOH	0.07 ± 0.05	3.51 ± 0.69	2.66 ± 0.26

4.4.3. AFM analysis of untreated and Tween 80-treated SAM substrates before and after cellulase adsorption

AFM was used to image both untreated and Tween 80-treated SAM substrates before and after exposure to cellulase solution. Representative images are shown in Figure 4.5. At least four images were collected for each substrate, and the surface roughnesses reported in Table 4.3 are means ± one standard deviation. The surface roughness of the SAM substrates was higher than that of the bare gold surface, especially in the case of SAM-CH_3. According to the literature, alkanethiol molecules dissolved in polar solvents induce corrosive defects or holes in the topmost layer of gold substrates,[25-28] which may result in an increase in surface roughness. It can be observed that a large amount of cellulase adsorbed as aggregates onto untreated SAM-CH_3 substrates, resulting in a significant increase in their surface roughness. In contrast, many fewer cellulase aggregates were present on untreated SAM-OH substrates, corresponding to the low cellulase surface concentration. It is also interesting to note that although the adsorbed amount of cellulase was low, the surface roughness of the SAM-OH nearly doubled. This observation agrees with the high dissipation increase for SAM-OH in the QCM-D experiments (Figure 4.1(b)), which suggests cellulase formed a floppy, viscous layer with high water content. The

cellulase aggregates on SAM-CH_3 substrates appear smaller than those on SAM-OH substrates. Because of the strong interaction between cellulase and the SAM-CH_3 substrates, cellulase formed smaller aggregates and adsorbed with greater surface coverage than on the SAM-OH substrates. Although QCM-D and SPR experiments indicated the largest amount of cellulase adsorbed onto untreated SAM-COOH substrates, cellulase did not form obvious aggregates on these substrates, and their mean roughness decreased after exposure to cellulase solution. Since electrostatic interactions are thought to be the dominant driving force for cellulase adsorption onto SAM-COOH substrates, the cellulase enzyme aggregates may disintegrate into the individual enzymes that adjust their conformation to interact with the negatively charged sites of the SAM-COOH substrates through positively charged amino acids such as lysine. Thus, a smooth enzyme monolayer might have been formed. This hypothesis is supported by the small dissipation increase for SAM-COOH in the QCM-D experiments (Figure 4.1(b)).

For Tween 80-treated SAMs, all three SAM substrates became smoother after exposure to Tween 80. Tween 80 may form a smooth layer on the substrates and decrease their surface roughness. For Tween 80-treated SAM-CH_3 substrates, few cellulase aggregates were observed, and the surface roughness remained the same before and after exposure to cellulase. This observation suggests Tween 80 effectively hindered the adsorption of cellulase. For cellulase adsorption onto Tween 80-treated SAM-OH, QCM-D, SPR and AFM images all indicated very limited amounts of adsorbed cellulase. Due to the extremely low surface coverage of cellulase aggregates on Tween 80-treated SAM-OH, the surface roughness of the substrate was almost identical before and after exposure to cellulase. However, a significant increase in ΔD was observed for the adsorbed cellulase layer (Figure 4.4 (b)). The enhanced dissipation may be due to the viscous nature of cellulase aggregates.

The morphology and mean surface roughness of cellulase-exposed Tween 80-treated SAM-COOH substrates were no different from those of cellulase-exposed untreated SAM-COOH substrates. Adsorbed Tween 80 was almost completely removed during the buffer rinse, the surfactant treatment on hydrophilic substrates had no significant effect on cellulase adsorption.

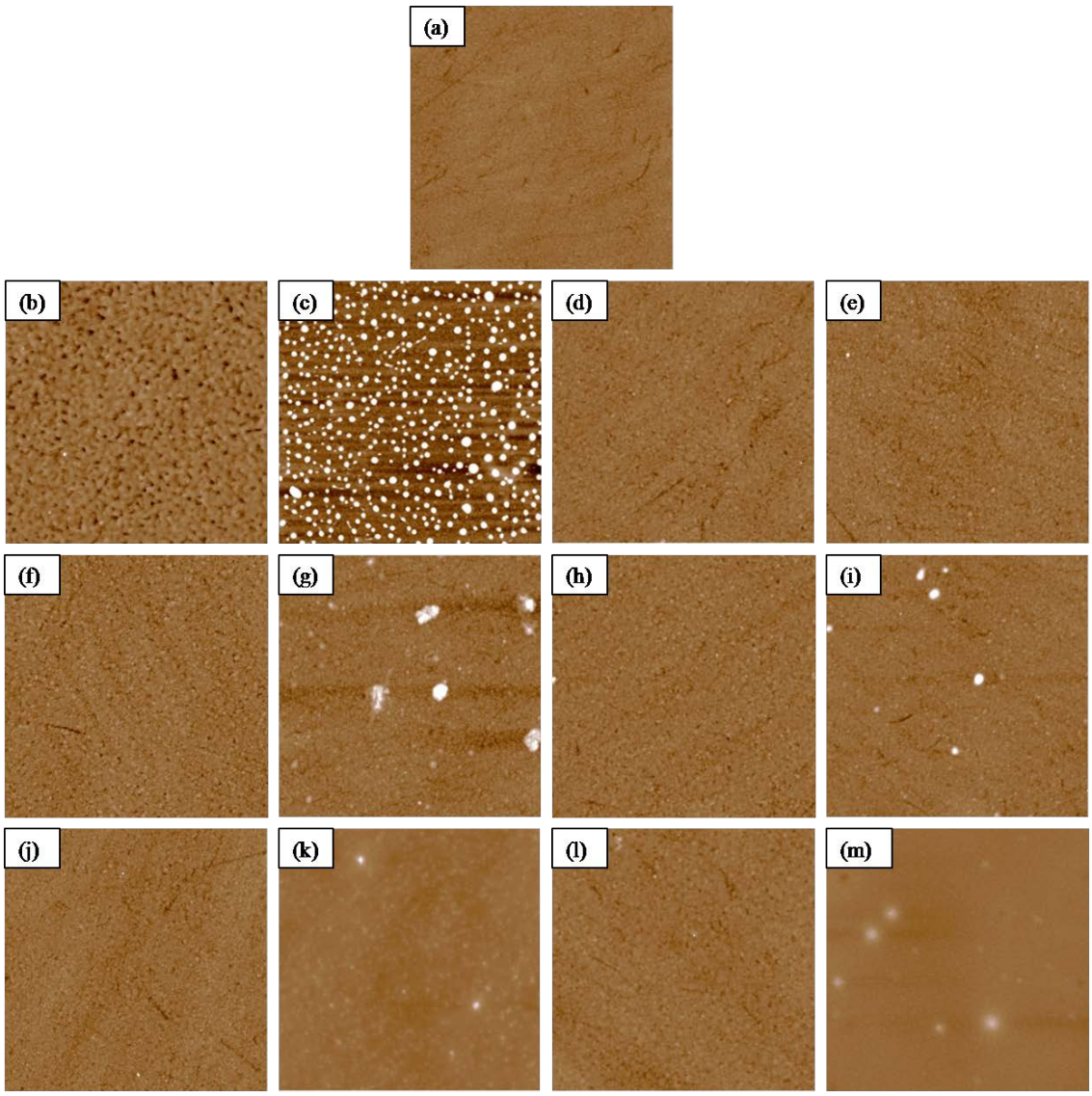

Figure 4.5. AFM height images: (a) Bare gold surface, (b) SAM-CH_3, (c) cellulase-exposed SAM-CH_3, (d) Tween 80-treated SAM-CH_3, (e) cellulase-exposed Tween 80-treated SAM-CH_3, (f) SAM-OH, (g) cellulase-exposed SAM-OH, (h) Tween 80-treated SAM-OH, (i) cellulase-exposed Tween 80-treated SAM-OH, (j) SAM-COOH, (k) cellulase-exposed SAM-COOH, (l) Tween 80-treated SAM-COOH and (m) cellulase-exposed Tween 80-treated SAM-COOH. The scan size and z-scale are 5μm × 5 μm and 30 nm for all images, respectively.

Table 4.3. Surface roughnesses of the SAM substrates before and after cellulase adsorption.

Substrate	Roughness (nm)
Bare gold	1.1 ± 0.1
SAM-CH_3	2.2 ± 0.2
Untreated SAM-CH_3 after exposure to cellulase solution	7.7 ± 0.4
Tween 80-treated SAM-CH_3	1.5 ± 0.1
Tween 80-treated SAM-CH_3 after exposure to cellulase solution	1.3 ± 0.1
SAM-OH	1.8 ± 0.1
Untreated SAM-OH after exposure to cellulase solution	3.2 ± 1.2
Tween 80-treated SAM-OH	1.5 ± 0.2
Tween 80-treated SAM-OH after exposure to cellulase solution	2.0 ± 0.4
SAM-COOH	1.4 ± 0.1
Untreated SAM-COOH after exposure to cellulase solution	0.8 ± 0.2
Tween 80-treated SAM-COOH	1.3 ± 0.1
Tween 80-treated SAM-COOH after exposure to cellulase solution	1.0 ± 0.3

4.5. Conclusions

Comparable amounts of cellulase adsorbed onto SAM-CH_3 and SAM-COOH substrates in the absence of a Tween 80 treatment. The driving force for cellulase adsorption onto SAM-CH_3 and SAM-COOH surfaces were attributed to van der Waals and electrostatic interactions, respectively. However, only a small amount of cellulase adsorbed onto SAM-OH substrates in the absence of a surfactant treatment, possibly because of weaker polar interactions, such as hydrogen bonding. These results suggest that cellulase adsorption onto lignin substrates may be

driven by either van der Waals or electrostatic interactions and that hydrogen bonding plays a limited role. Cellulase adsorbed onto SAM-CH_3 substrates formed smaller aggregates with the lowest water content, compared to cellulase adsorbed onto SAM-OH substrates which had the highest water content or SAM-COOH surfaces where adsorbed cellulase formed a smooth layer.

Tween 80 had strong, presumably van der Waals interactions with SAM-CH_3 substrates and effectively hindered cellulase adsorption. However, Tween 80 had almost no effect on cellulase adsorption onto SAM-OH and SAM-COOH substrates because most of the Tween 80 already adsorbed reversibly.

4.6. Acknowledgements

This project was supported in part by the Center for LignoCellulose Structure and Formation, an Energy Frontier Research Center funded by the U.S. Department of Energy, Office of Science, Office of Basic Energy Sciences under Award Number DE-SC0001090. The project was also partially supported by the National Science Foundation (CHE-0724126), the Macromolecules and Interfaces Institute at Virginia Tech, and the U.S. Department of Transportation through the Southeastern Sun Grant Center.

4.7. References

(1) Himmel, M. E.; Ding, S.-Y.; Johnson, D. K.; Adney, W. S.; Nimlos, M. R.; Brady, J. W.; Foust, T. D. *Science (Washington, DC, U. S.)* **2007**, *315*, 804.

(2) Lynd, L. R. *Annual Review of Energy and the Environment* **1996**, *21*, 403.

(3) Yang, B.; Wyman, C. E. *Biotechnol. Bioeng.* **2006**, *94*, 611.

(4) Berlin, A.; Balakshin, M.; Gilkes, N.; Kadla, J.; Maximenko, V.; Kubo, S.; Saddler, J. *J. Biotechnol.* **2006**, *125*, 198.

(5) Bura, R.; Mansfield, S.; Saddler, J.; Bothast, R. *Appl. Biochem. Biotechnol.* **2002**, *98-100*, 59.

(6) Wingren, A.; Galbe, M.; Zacchi, G. *Biotechnol. Prog.* **2003**, *19*, 1109.

(7) Gregg, D. J.; Boussaid, A.; Saddler, J. N. *Bioresour. Technol.* **1998**, *63*, 7.

(8) Tu, M.; Pan, X.; Saddler, J. N. *J. Agric. Food Chem.* **2009**, *57*, 7771.

(9) Chernoglazov, V. M.; Ermolova, O. V.; Klyosov, A. A. *Enzyme Microb. Technol.* **1988**, *10*, 503.

(10) Converse, A.; Ooshima, H.; Burns, D. *Appl. Biochem. Biotechnol.* **1990**, *24-25*, 67.

(11) Jiang, F., Virginia Polytechnic Institute and State University, 2011.

(12) Castanon, M.; Wilke, C. R. *Biotechnol. Bioeng.* **1981**, *23*, 1365.

(13) Eriksson, T.; Börjesson, J.; Tjerneld, F. *Enzyme Microb. Technol.* **2002**, *31*, 353.

(14) Kristensen, J. B.; Börjesson, J.; Bruun, M. H.; Tjerneld, F.; Jørgensen, H. *Enzyme Microb. Technol.* **2007**, *40*, 888.

(15) Börjesson, J.; Peterson, R.; Tjerneld, F. *Enzyme Microb. Technol.* **2007**, *40*, 754.

(16) Sipos, B.; Dienes, D.; Schleicher, Á.; Perazzini, R.; Crestini, C.; Siika-aho, M.; Réczey, K. *Enzyme Microb. Technol.* **2010**, *47*, 84.

(17) Qing, Q.; Yang, B.; Wyman, C. E. *Bioresour. Technol.* **2010**, *101*, 5941.

(18) Tsai, M.-Y.; Lin, J.-C. *J. Biomed. Mater. Res.* **2001**, *55*, 554.

(19) Berlin, A.; Gilkes, N.; Kilburn, D.; Bura, R.; Markov, A.; Skomarovsky, A.; Okunev, O.; Gusakov, A.; Maximenko, V.; Gregg, D.; Sinitsyn, A.; Saddler, J. *Enzyme Microb. Technol.* **2005**, *37*, 175.

(20) Berlin, A.; Gilkes, N.; Kurabi, A.; Bura, R.; Tu, M.; Kilburn, D.; Saddler, J. *Appl. Biochem. Biotechnol.* **2005**, *121*, 163.

(21) Palonen, H.; Tjerneld, F.; Zacchi, G.; Tenkanen, M. *J. Biotechnol.* **2004**, *107*, 65.

(22) Noy, A.; Vezenov, D. V.; Rozsnyai, L. F.; Lieber, C. M. *J. Am. Chem. Soc.* **1997**, *119*, 2006.

(23) van, d. V. E. W.; Hadziioannou, G. *Langmuir* **1997**, *13*, 4357.

(24) Hedin, J.; Loefroth, J.-E.; Nyden, M. *Langmuir* **2007**, *23*, 6148.

(25) Cao, Z.; Zhang, L.; Guo, C.-Y.; Gong, F.-C.; Long, S.; Tan, S.-Z.; Xia, C.-B.; Xu, F.; Sun, L.-X. *Materials Science and Engineering: C* **2009**, *29*, 1051.

(26) Chidsey, C. E. D.; Loiacono, D. N. *Langmuir* **1990**, *6*, 682.

(27) Edinger, K.; Goelzhaeuser, A.; Demota, K.; Woell, C.; Grunze, M. *Langmuir* **1993**, *9*, 4.

(28) Edinger, K.; Grunze, M.; Woll, C. *Ber. Bunsen-Ges. Phys. Chem. Chem. Phys.* **1997**, *101*, 1811.

CHAPTER 5

Conclusions

With respect to the research objectives stated in Chapter 1, the following conclusions can be drawn:

The adsorption of xyloglucan onto cellulose is driven by non-specific hydrogen bonding. Accessible surface area of the cellulose films plays a significant role in xyloglucan adsorption. However, morphology and surface charge of cellulose substrates have limited impact on xyloglucan adsorption. Amorphous, regenerated cellulose films are well suited for comparing the relative strengths of interactions between cellulose and other matrix polymers. Nanocrystalline cellulose films may be useful in building nanoscale models of plant cell walls and biomimetic composites.

Cellulase adsorption onto lignin substrates may be driven by both van der Waals and electrostatic interactions. Moreover, hydrogen bonding plays a lesser role in cellulase adsorption. Tween 80 has strong interactions with SAM-CH_3 substrates and effectively hinders the adsorption of cellulase. However, Tween 80 has almost no effect on the adsorption of cellulase onto SAM-OH and SAM-COOH substrates because of reversible Tween 80 adsorption to these substrates.

Appendix A

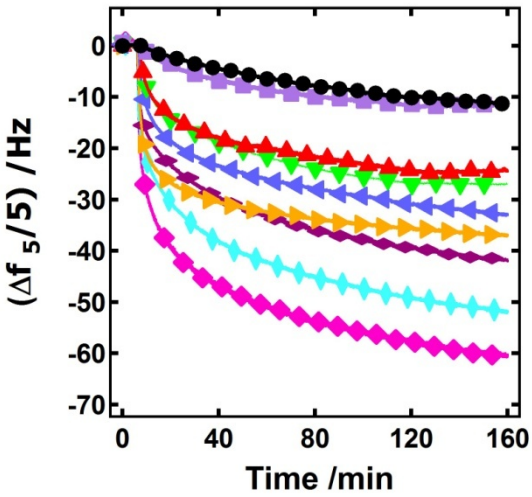

Figure A.1. Representative data for the adsorption of xyloglucan solutions of varied concentration onto DNC by QCM-D (n = 5). Symbols correspond to XG concentrations of (●) 1 mg·L^{-1}, (■) 5 mg·L^{-1}, (▲) 10 mg·L^{-1}, (▼) 25 mg·L^{-1}, (◀) 50 mg·L^{-1}, (▶) 75 mg·L^{-1}, (◆) 100 mg·L^{-1}, (✦) 250 mg·L^{-1}, and (◆) 500 mg·L^{-1}.

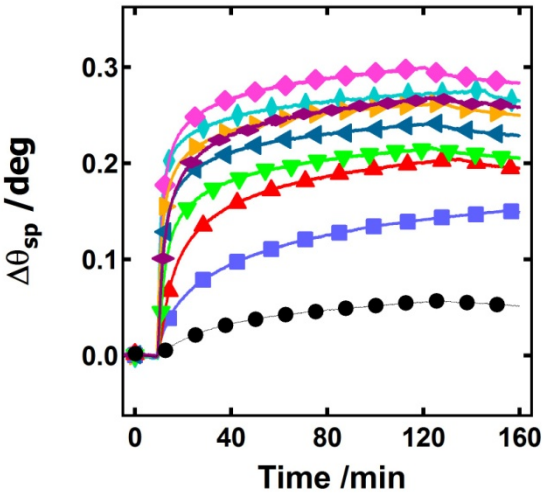

Figure A.2. Representative data for the adsorption of xyloglucan solutions of varied concentration onto DNC by SPR (n = 5). Symbols correspond to XG concentrations of (●) 1 mg·L^{-1}, (■) 5 mg·L^{-1}, (▲) 10 mg·L^{-1}, (▼) 25 mg·L^{-1}, (◀) 50 mg·L^{-1}, (▶) 75 mg·L^{-1}, (◆) 100 mg·L^{-1}, (✦) 250 mg·L^{-1}, and (◆) 500 mg·L^{-1}.